*Thèse d'habilitation à diriger des recherches*
*Contribution en Signal, Image et Instrumentation pour l'Astronomie*

# Annexe D. Contribution à la technique SCIDAR: restauration de profils verticaux de vent et de turbulence atmosphérique

*Habilitation thesis, "Accreditation to supervise research"*
*Contribution to Signal, Image & Instrumentation in Astronomy*

# Appendix D. Contribution to the SCIDAR technique: wind and atmospheric turbulence vertical profile restoration

Jean-Louis Prieur

*Version March 31, 2014*

Mots clés:
Turbulence: atmosphérique, scintillation, coefficient de structure d'indice, profils verticaux de vent, échelle externe
Problèmes inverses: CLEAN, Maximum Entropy
Techniques: SCIDAR, SCIDAR généralisé, Optique adaptive, Interféromètre à double champ

Keywords:
Turbulence: atmospheric, scintillation, refractive-index structure coefficient, wind vertical profiles, outer scale
Inverse problems: CLEAN, Maximum Entropy
Techniques: SCIDAR, Generalized SCIDAR, Adaptive optics, Dual-Field interferometer

# Contents

## Foreword

A "conventional" SCIDAR experiment was performed in September 1998 with PISCO and the 2m Telescope Bernard Lyot at Pic du Midi. From the observation of two binary stars, $\gamma$ Ari and $\gamma$ Del we derived vertical profiles of the optical turbulence and wind velocity for the altitudes in the range 3 km to about 18 km (Prieur et al., 2001).

This was the first time that PISCO was used for SCIDAR observations. For processing those data we developed a specific reduction software with a new approach based on the CLEAN algorithm. We then adapted this method to "generalized" SCIDAR observations and processed them with a fully automatic data reduction procedure (Prieur et al., 2004). In this appendix, we describe in detail the CLEAN method that we proposed for the inversion of vertical profiles of the refractive index structure $C_{\mathrm{N}}^2(h)$ that characterize the turbulence and of the wind parameters. An index (see II.5) at the end of this appendix was build to facilitate its understanding.

# Chapter I

# SCIDAR

## I.1 Presentation of the SCIDAR technique

A direct estimate of the vertical distribution of turbulence and its time variations can be obtained through the observation of stellar-light irradiance fluctuations in the entrance pupil of a telescope. Indeed, the coherence radius of the scintillation pattern due to a single diffractive layer depends on its distance to the entrance pupil of the telescope, and varies as the square root of this distance. The experiment conducted at Nice Observatory in 1974 by Rocca, Roddier and Vernin (Rocca et al., 1974), on spatio-temporal correlation of scintillations, has shown that reliable results could be obtained with the observation of a double star and the so-called spatio-angular correlation of the compound scintillation pattern. Since then, the technique is known as SCIDAR, for SCIntillation Detection And Ranging. It has then been used on different telescopes in many astronomical observatories for site testing, as a complement to seeing measurements (for a review, see Avila (1998a)). Although the SCIDAR spatial resolution along the line of sight cannot compete with *in situ* measurements for detailed studies of the turbulence distribution, it provides a instantaneous view of the whole vertical profile of turbulence, which is not possible with balloon sounding. The SCIDAR measurements might thus bring some new insights on turbulence lifetime at different altitudes, from a few kilometers upwards.

In collaboration with Gérard Daigne (Obs. Bordeaux, France) and Rémy Avila (OCA, France) we started a SCIDAR observing program with PISCO (Prieur et al., 1998) at Pic du Midi in 1998. Our purpose was not site testing, but it was a preliminary investigation of SCIDAR technique as a support to ground-based differential astrometry. Indeed, optical turbulence produced high in the atmosphere was expected to be the main limiting factor in narrow-angle measurements that were going to be performed with dual-field interferometers (DFI) (Shao & Colavita, 1992; Colavita , 1994). Its deteriorating effects had to be clearly evaluated before one can try and reduce them. Furthermore, since the SCIDAR technique can be performed with a telescope aperture about the size of the entrance pupil of an optical interferometer observing in the near-IR range ($D \simeq 1.5$ m), it could be a unique technique, along with DFI, for probing and tracking turbulence distribution and wind velocity. We describe here the main theoretical aspects of our study. More details can be found in Prieur et al. (2001) and Daigne et al. (2000).

Numerous *in situ* measurements of temperature fluctuations carried out with balloon sounding had shown that regions responsible for optical turbulence were usually localized

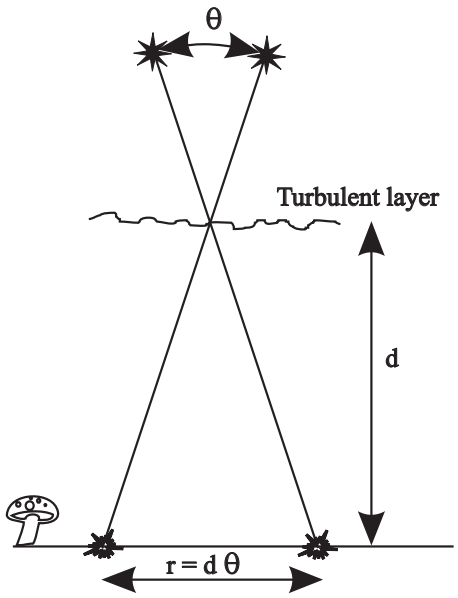


Figure I.1: SCIDAR basic principle: schematic of the irradiance fluctuations and their correlation with double star observation.

in a few thin layers, about 10-50 meters thick (Coulman et al., 1995). Unfortunately, little (Avila et al., 1998b) was known about their temporal variations, on time scales of one minute or so, which are typical integration times for measurements with DFI's in the near IR, see *e.g.* descriptions of the Palomar Tesbed Interferometer or PTI (Colavita et al., 1999; Lane et al., 2000).

# I.2 Brief theory of SCIDAR

## I.2.1 Basic principle with a single turbulent layer

Classical SCIDAR is based on the observation of irradiance fluctuations of a double star at ground level (Rocca et al., 1974; Caccia et al., 1987; Avila, 1998a). With a single turbulent layer at distance $d_j$ (see Fig. I.1), two stars with angular separation $\overrightarrow{\theta}$ cast to the ground similar diffraction patterns shifted by $\overrightarrow{r_j} = d_j \overrightarrow{\theta}$. The covariance $C_2(\overrightarrow{\rho})$ of the irradiance fluctuations exhibit two secondary peaks at $\pm \overrightarrow{r}_j$:

$$C_2(\overrightarrow{\rho}) = A\, C_1(\overrightarrow{\rho}) + B \left[ C_1(\overrightarrow{\rho} + d_j \overrightarrow{\theta}) + C_1(\overrightarrow{\rho} - d_j \overrightarrow{\theta}) \right] \tag{I.1}$$

$$\text{with } A = (1+\alpha^2)/(1+\alpha)^2 \quad \text{and } B = \alpha/(1+\alpha)^2 \tag{I.2}$$

where $\alpha$ is the brightness ratio of the binary components (related to the magnitude difference $\Delta m$ by $\alpha = 10^{-0.4\Delta m}$) and $C_1(\overrightarrow{\rho})$ is the normalized covariance function of the irradiance fluctuations for single star observations.

$C_1(\overrightarrow{\rho})$ is the Fourier transform of the power spectrum $W_I$ of the irradiance fluctuations at ground level, given by Roddier (1981):

$$W_I(\overrightarrow{f}) = 4\, W_\Phi(\overrightarrow{f}) \sin^2(\pi \lambda d_j f^2) \tag{I.3}$$

where $\lambda$ is the observed wavelength and $W_\Phi$ is the power spectrum for the phase fluctuations at the level of the layer, generally assumed to follow Kolmogorov statistics. In that case $C_1(\rho)$ is isotropic and proportional to $J_j$, the *optical turbulence factor* (Tokovinin, 1997) of the thin layer, which is related to the refractive index structure parameter, $C_N^2(h)$, by:

$$J_j = \int_{h_j-\delta h_j/2}^{h_j+\delta h_j/2} C_N^2(h)\,\mathrm{d}h, \tag{I.4}$$

$\delta h_j$ being the thickness of the layer. With a line of sight at zenith angle $z$, the observed turbulence factor is $\tilde{J}_j = J_j \sec(z)$. The expression of $C_1(\rho)$ is then:

$$C_1(\rho) = \tilde{J}_j\, K(\rho, d_j) \tag{I.5}$$

with:

$$K(\rho, d_j) = 0.243\, k^2 \int_0^\infty f^{-8/3} \sin^2(\pi\lambda d_j f^2)\, J_0(2\pi f\rho)\,\mathrm{d}f. \tag{I.6}$$

It is plotted in Fig. I.2 for different distances to the turbulent layer and was observed in the experiment reported here, with its negative feet. The correlation radius of the irradiance fluctuations is about the radius of the first Fresnel zone $\sqrt{\lambda d/2\pi}$ (Tatarskii, 1961), so that spatial resolution along the line of sight (i.e., the ability to separate two turbulent layers of equal $J$ factor) is given by:

$$\Delta d_j \simeq \frac{0.78\sqrt{\lambda d_j}}{\theta}. \tag{I.7}$$

We derived the value of 0.78 from the FWHM (Full Width at Half Maximum) of the curves $C_1(\rho)$ in Fig. I.2.

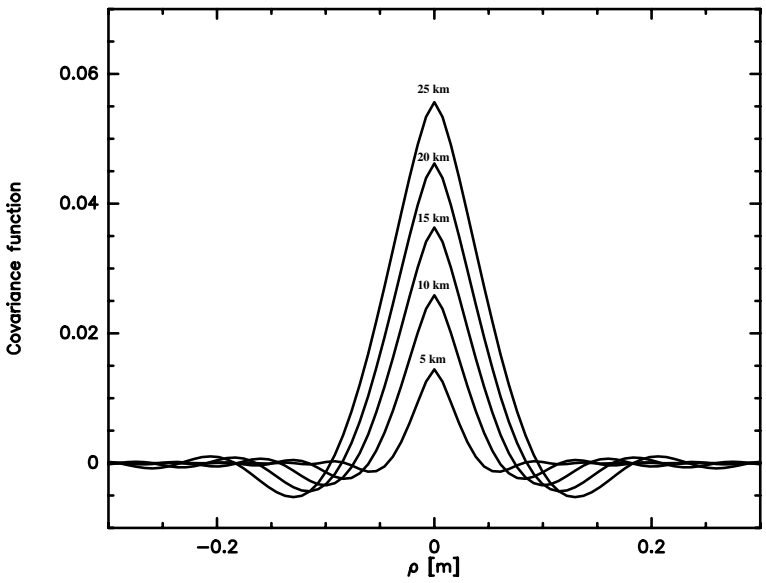


Figure I.2: Covariance function $C_1(\rho)$ of irradiance due to a single turbulent layer, with optical turbulence factor $J = 3.10^{-14}$ [m$^{1/3}$], at different distances: $h$ = 5, 10, 15, 20, 25 km. The wavelength is $\lambda = 0.53\,\mu$m.

### I.2.2 Principle with a vertical distribution of turbulence

Several turbulent layers along the line of sight are statistically independent, so that the different contributions will sum in quadratic form. More precisely, the power spectra of the relative irradiance fluctuations $\delta I/I$ will add (Tatarskii, 1961; Roddier, 1981). In SCIDAR measurements, only a few turbulent layers will contribute to the covariance function at a given $\rho$ value, away from the central peak, so that the weak-scintillation approximation can be safely used: the covariance function $C_{sci}(\overrightarrow{\rho})$ outside the central peak is estimated from irradiance fluctuations instead of from the logarithm of the irradiance.

With a continuous distribution of turbulence along the line of sight, the covariance profile in the $\theta$ direction will be:

$$C_{sci}(\rho) = B \sec(z) \int_0^\infty K\left(\rho, h \sec(z)\right) C_N^2(h)\, \mathrm{d}h \tag{I.8}$$

which is a Fredholm-type integral with kernel $K(\rho, h\sec(z))$. A maximum entropy method (MEM) can be used to recover the distribution of the index structure parameter (Avila, 1998a).

An alternative is to consider a multi-layer model with a discrete distribution of turbulence along the line of sight:

$$C_{sci}(\overrightarrow{\rho}) = B \sum_j \tilde{J}_j\, K\left(|\overrightarrow{\rho} - \overrightarrow{r}_j|, d_j\right) \tag{I.9}$$

which can be solved in 2-D space with a CLEAN algorithm.

### I.2.3 Limited pupil size and sensitivity

In practice, the covariance function is estimated with a limited pupil size, and the incoming radiation has to be multiplied by a pupil function $P(\overrightarrow{r})$ ($P$=0 or 1). Experimentally, the normalized covariance function of irradiance $C_2(\overrightarrow{\rho})$ will be approximated with:

$$C_2(\overrightarrow{\rho}) \approx C_{\delta I}(\overrightarrow{\rho}) / C_{I_0}(\overrightarrow{\rho}) \tag{I.10}$$

where $C_{I_0}(\overrightarrow{\rho})$ is the covariance of the average pupil irradiance function $I_0(\overrightarrow{\rho})$ estimated on a large ensemble of frames and $C_{\delta I}(\overrightarrow{\rho}) = \langle [I(\overrightarrow{\rho}) - I_0(\overrightarrow{\rho})]^2 \rangle$ is the covariance of the irradiance fluctuations, per frame, relative to $I_0(\overrightarrow{\rho})$.

Let us now estimate the expected limiting sensitivity of our measurements. The statistical rms noise of $C_{sci}(\rho)$, per frame is given by Tokovinin (1997):

$$\Delta C_{sci}(\rho) = (C_2(0) + 1/N_{ph}) / \sqrt{M(\rho)} \tag{I.11}$$

where $N_{ph}$ is the mean number of photons per coherence area and $C_2(0)$ is the intensity dispersion ($= A\sigma_I^2$, where $\sigma_I^2$ is the scintillation index). The read-out noise and/or recording noise are not considered here. The number of independent cells $M(\rho)$ is given by the ratio of the overlapping pupil area $S$ to the coherence area of the scintillation patterns. Following the detailed analysis performed by Vernin & Azouit (1983), we take it as the Fresnel zone area ($\lambda d_0/2$) where $d_0$ is the distance of the dominant turbulent layer which governs the size of the noisy structures in the covariance function. With circular aperture of diameter $D$, the

overlapping pupil area is $S(x) = f(x)\,D^2/2$ with $x = \rho/D$ and $f(x) = \arccos(x) - x(1 - x^2)^{1/2}$. Hence:

$$M(\rho) = \frac{D^2 f(x)}{\lambda\, d_0}. \tag{I.12}$$

From Eq. I.9 applied at $\rho = r_j$, the location of the maximum of the $j$th component, we deduce the expression of the uncertainty of the optical turbulence factor, for the layer at distance $d_j$:

$$\Delta\tilde{J}_j = \frac{\Delta C_{sci}(r_j)}{B\,K(0, d_j)}. \tag{I.13}$$

With $K(0, d_j) = 19.12\,\lambda^{-7/6} d_j^{5/6}$, we obtain a general expression for the rms noise per frame in SCIDAR measurements:

$$\Delta\tilde{J}_j = \frac{5.23\,10^{-2}\lambda^{5/3} d_j^{-5/6} d_0^{1/2}(C_2(0) + 1/N_{ph})}{B\,D\sqrt{f(x)}} \tag{I.14}$$

with $x = \theta d_j/D$. For $N$ independent frames, $\Delta\tilde{J}_j$ is multiplied by $N^{-1/2}$. It is plotted in Fig. I.3 in terms of the distance $d_j$ to the turbulent layer for $N = 1500$, $B = 0.25$ (i.e., components of equal magnitude) and $\lambda = 0.53\,\mu$m. The coefficients $(C_2(0) + 1/N_{ph}) = 0.15$ and $d_0 = 17$ km are close to the measured values with our PISCO observations (Sect. I.3.3). Hence with aperture diameters larger than 1.5 m, the altitude range above $\sim 9$ km can be probed with an uncertainty smaller than $10^{-15}$ [m$^{1/3}$] for the turbulence factor.

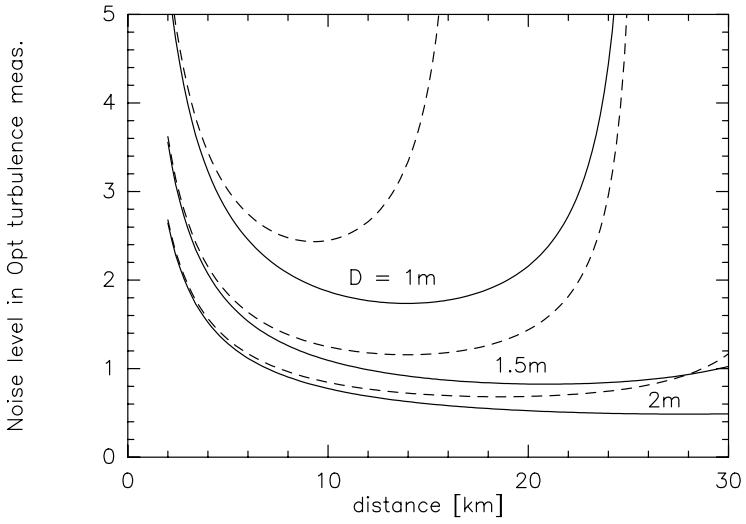


Figure I.3: Noise level (rms) in SCIDAR measurements of the optical turbulence factor $J$ (in $10^{-15}$m$^{1/3}$), with different circular apertures, whose diameter $D$ is in the range 1–2 m. The angular separation of the observed binary star is 8"(solid line), or 12"(dashed line).

## I.3 Derivation of vertical profiles of turbulence

Using the SCIDAR observations made with PISCO in 1998, we developed a new method for deriving vertical profiles of turbulence. This is described in the present section and in (Prieur et al., 2001).

Theoretically, all the information needed to retrieve $C_N^2(h)$ is contained in a radial section of $C_2(\overrightarrow{\rho})$, along the double star separation (cf. Sect. I.2.1). In order to eliminate the central peak which contains the uncorrelated noise and where the contribution of each layer is indistinguishable from that of the others, since they are added, we compute the difference of the sections of the measured auto-correlation function parallel and perpendicular to the star separation, $C_2^{\parallel}(\rho)$ and $C_2^{\perp}(\rho)$ respectively. This quantity can be written as Eq. I.8 plus an additive noise function $N(\rho)$:

$$C_2^{\parallel}(\rho) - C_2^{\perp}(\rho) = C_{sci}(\rho) + N(\rho) \tag{I.15}$$

The resulting equation is of Fredholm type.

### I.3.1 Derivation of $C_N^2$ profiles with a 1-D Maximum-Entropy-Method

For deriving turbulence vertical profiles, we first used the Maximum-Entropy-Method (MEM) that is implemented in J. Vernin and R. Avila's CN2 program (Avila, 1998a), This method was originally developed by Vernin (1984).

In Vernin's method, Equation I.15 is inverted by finding a solution that maximizes the joint entropy of the unknown quantities $C_N^2(h)$ and $N(\rho)$. The entropy is calculated analytically. Its maximization, using the Lagrange multipliers method, leads to a system of non-linear equations, which is solved by a Newtonian iterative algorithm. In each iteration, an auto-correlation function is calculated from the retrieved $C_N^2(h)$ and $N(\rho)$. The iterations are stopped when the difference between this calculated auto-correlation and the measured one has a variance which is less than the estimated variance of the noise.

### I.3.2 Derivation of $C_N^2$ profiles with our 2-D CLEAN method

For solving Equation I.15, we have used a CLEAN approach (Schwarz, 1978). We have written an object-orientated program that directly works on the 2-D autocorrelation function of the irradiance fluctuations, to take advantage of the two-dimensional information and improve the robustness of the inversion (Avila and Vernin's MEM program works on a slice of the autocorrelation only).

This program is basically based on the CLEAN algorithm. At step $k = 0$, the 2-D residual map is initialized with the mean autocorrelation function of the irradiance fluctuations.

We then start an iterative loop on $k$. For each step $k$, we look for the location $\overrightarrow{\rho}_k$ and value $z_k$ of the maximum in the 2-D residual map. We then compute $d_k$, its corresponding distance along the line of sight, and subtract a fraction of the 2-D function $C_{sci}(\overrightarrow{\rho}, d_k) = B\,\tilde{J}_k\,K(\overrightarrow{\rho}, d_k)$ from the residual map, with:

$$\tilde{J}_k = \frac{z_k}{19.12\,\lambda^{-7/6}\,d_k^{5/6}\,B} \tag{I.16}$$

where B is the coefficient defined in Eq. I.1.

The maxima are searched within two regions of the $C_2(\overrightarrow{\rho})$ image: the "binary zone", i.e., a sector centered on the direction joining the two components of the binary and whose opening angle is adjusted to the width of the covariance function $C_{sci}(\rho)$ (cf. Fig. I.2), and the "test zone", i.e. a region further out (see Fig. I.4c) which is used to determine the noise level of the image.

If this noise level is not reached, we increment $k$ and proceed in the iterative loop.

When this noise level is reached, the process is stopped by exiting from the loop.

We then output the final residual map (e.g., Fig. I.4c) and the list of CLEAN components ($\tilde{J}_k$). We then follow the general scheme used in radio-astronomy (Schwarz, 1978), and convolve the CLEAN components by a "CLEAN beam", generally Gaussian, to generate the CLEAN map (e.g., Fig. I.4b).

The final $C_N^2$ profile is obtained by the convolution of the list ($\tilde{J}_k$) with a set of normalized Gaussian functions centered at $d_k$ whose sigma is equal to the resolution $\Delta d_k$ of the SCIDAR measurements at this distance $d_k$:

$$C_N^2(d) \approx \sum_k \tilde{J}_k \times \frac{1}{\Delta d_k \sqrt{2\pi}} \exp\left(-\frac{(d-d_k)^2}{2\Delta d_k}\right) \tag{I.17}$$

with $\Delta d_k = 0.34\sqrt{\lambda d_k}/\theta$ (cf. Eq. I.7 which gives $\Delta_j$ the FWHM, i.e., $2.3\sigma$ of a Gaussian).

One could object that this operation degrades the resolution, but (i) this convolution is part of the CLEAN algorithm and regularizes it and (ii) it takes into account the physics governing the SCIDAR detection, more precisely, the Fresnel propagation (cf. Sect. I.2). A higher resolution as in the case of our current implementation of MEM (see Fig. I.5) would actually be a "super-resolution" relative to the data and possibly subject to artifacts.

### I.3.3 Limiting sensitivity of our observations

As shown in Fig. I.6, in the extraction process of turbulence distribution with CLEAN, the components cannot be detected below some sensitivity threshold which is dependent on distance.

Since the size of the components increases with the distance as $d^{1/2}$, the curve of detection with constant SNR (solid line in Fig. I.6) can be obtained by multiplying the rms noise $\Delta\tilde{J}_j$ (as given in Eq. I.14) by $(d_j/d_0)^{1/2}$ (dashed line in Fig. I.6). As in Sect. I.2.3, we assume here a constant area for the noise fluctuations which is proportional to the distance $d_0$ of the dominant turbulent layer responsible for scintillations (respectively 17 and 12 km for $\gamma$ Ari and $\gamma$ Del in Fig. I.5).

In Fig. I.6, we see that the model well fits the variations of sensitivity threshold for $\gamma$ Ari. Actually, a high sensitivity of a few $10^{-16}$ m$^{1/3}$ has been reached for the upper most turbulent layers. Probing the layers below $\sim$ 8 km would have required "generalized" SCIDAR but in that case the scintillation index would have increased because of the contribution of the lower layers. Hence the noise level would have been larger.

### I.3.4 Temporal filtering

The finite integration time $\tau$ of the measurement causes an attenuation of the signal compared to the case of an "instantaneous" measurement which was assumed in Sect. I.2. Let $\overrightarrow{V_j}$ be the wind velocity of the turbulent layer at a distance $d_j$. Assuming a frozen turbulence, the $K$ function defined in (Eqs. I.5 and I.6) becomes Tokovinin (2002):

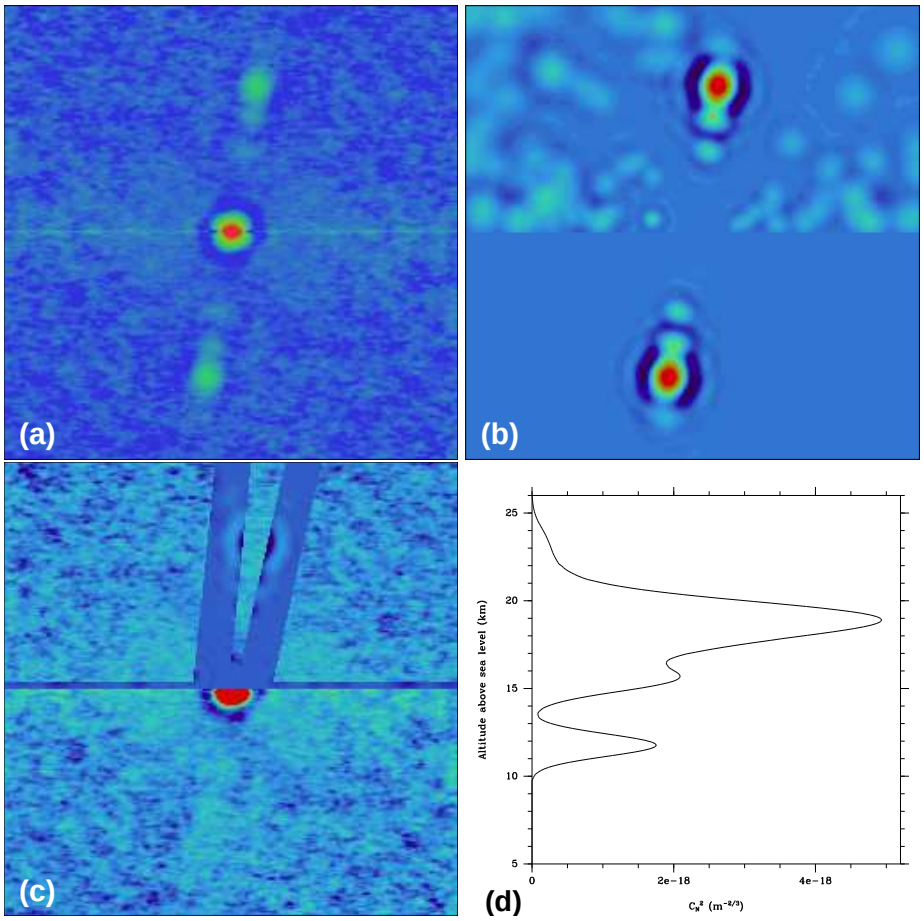


Figure I.4: Example of $C_N^2$ inversion of $C_2(\rho)$ function **(a)** of $\gamma$ Ari with the CLEAN derived method. **(b)**: clean image; **(c)**: residuals; **d**: restored $C_N^2$ profile. For **(b)** and **(c)**, the upper part shows all the clean components within the "binary" and the "test" zone, the bottom part shows the components selected within the "binary" zone only.

$$K(\overrightarrow{\rho}, d_j, \overrightarrow{V_j}\tau) = 1.53\,\lambda^{-2} \int f^{-11/3}\,\sin^2(\pi\lambda d_j f^2) \times \mathrm{sinc}^2(\overrightarrow{f}\cdot\overrightarrow{V_j}\tau)\,\exp(2i\pi\overrightarrow{f}\cdot\overrightarrow{\rho})\,\mathrm{d}\overrightarrow{f} \quad \text{(I.18)}$$

This relation is valid as long as $V_j\tau$ is much smaller than the diameter of the pupil. Fig. I.7 shows that the value of the central peak $K(\overrightarrow{0}, d_j, \overrightarrow{V_j}\tau)$ decreases significantly from its theoretical value of one as soon as $V_j\tau > 0.05$ m with a larger effect for the lower turbulent layers. Using (Eq. I.18), the attenuation was computed for the secondary peaks of $\gamma$ Ari with $\tau$=3 msec in Table I.1. The effect is significant for the layers at altitudes in the range 10–15 km which have high velocity winds. Likewise, for $\gamma$ Del, with a turbulent layer at 12 km and $\tau$=2 msec, the attenuation factor of the central peak is ∼0.5. Note that the $K$ attenuation factor of Table I.1 is that of the peak, not of the integral of the useful signal in the covariance plane, so that the "Corrected $\tilde{J}$ amplitude" should be taken as an upper bound to the detected turbulence factor.

Using (Eq. I.18), we also computed the deformation of the 2-D profile of the covariance

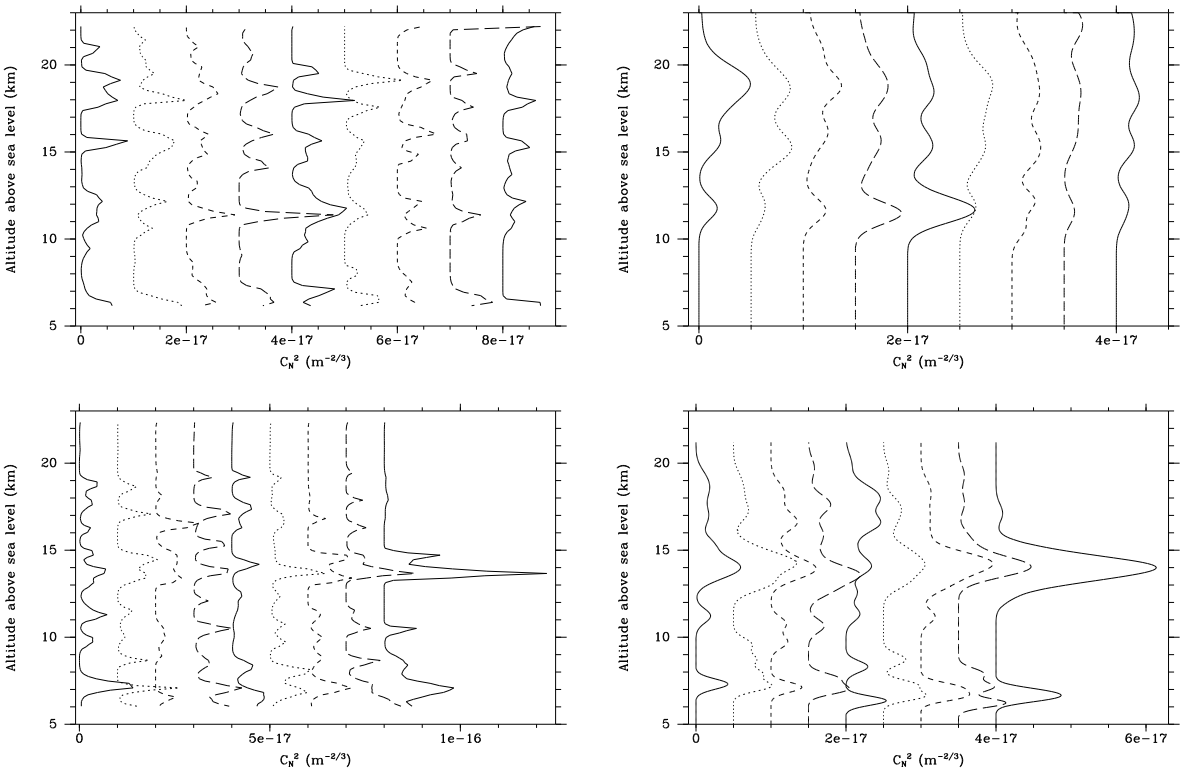


Figure I.5: SCIDAR observations with PISCO: set of $C_N^2$ profiles computed with $\gamma$ Ari (top) and $\gamma$ Del (bottom) (every 30 seconds) with MEM (left) and with CLEAN (right).

function along two directions: parallel to the wind and perpendicular to it (Fig. I.8). It appears that the profile is elongated along the direction of the wind and nearly unaffected perpendicularly. This is visible in the experimental $C_2(\overrightarrow{\rho})$ functions: the secondary peaks for altitudes at $\sim$12 km are elongated along the wind direction (e.g., Fig. I.4a). A possible improvement of our 2-D CLEAN algorithm would be to take into account the actual shape of the profile, elongated along the wind direction.

### I.3.5 Contribution to the seeing from different altitudes

The FWHM seeing is $s = \lambda/r_0$, where $r_0$ is the Fried parameter that can be computed with the following equation:

$$r_0 = \left[ 0.423 \left( \frac{2\pi}{\lambda} \right)^2 \sum_j J_j \right]^{-3/5}, \tag{I.19}$$

The total optical turbulence factor is $\tilde{J}_T = \sum_j J_j$.

### I.3.6 Conclusions about our work on the SCIDAR observations with PISCO

The PISCO speckle camera of *Observatoire Midi-Pyrénées* has thus produced SCIDAR measurements for the first time in 1998 and allowed the derivation of $C_N^2$ and wind profiles.

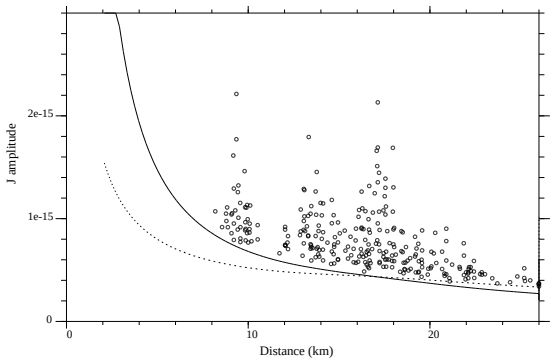


Figure I.6: $\tilde{J}$ amplitude of the components (small circles) detected with the CLEAN algorithm along the different observing sequences. The sensitivity threshold of our SCIDAR observations is shown as a solid curve. The dashed curve is the noise floor as given by (Eq. I.14) for the TBL ($D$=2 m plus central obscuration). Observations with PISCO in 1998: $\gamma$ Ari with $\sigma_I^2$=0.14, $N_{ph}$=110 photons and $d_0$=17 km

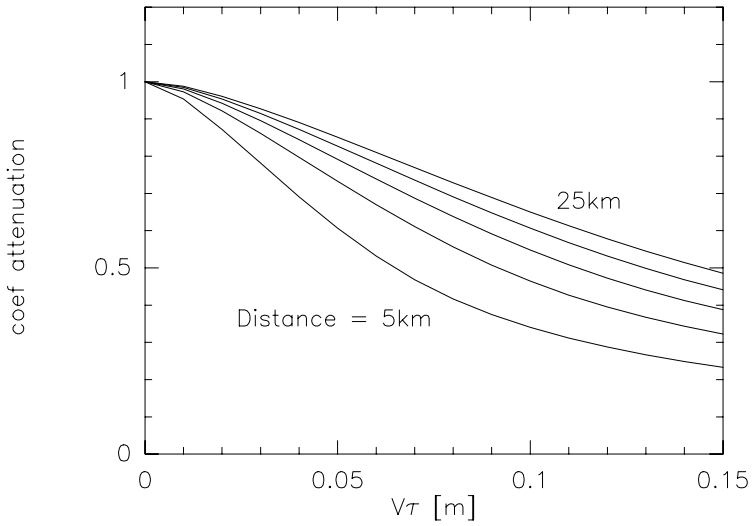


Figure I.7: Attenuation factor of the central peak of the scintillation covariance function due to the finite integration time of the measurements, for distance values of the turbulent layer in the range 5–25 km.

Our implementation of the CLEAN algorithm on the 2-D $C_2(\overrightarrow{\rho})$ function showed a higher robustness to the noise which is suitable for the analysis of the time variations. The other traditional MEM approach would also gain from a full use of the 2-D data instead of a slice only. The elongation of the scintillation covariance function due to strong winds in altitude also suggests that a full 2-D processing taking this effect into account would be desirable.

Following the CLEAN approach, an automatic procedure was developed for measuring wind parameters in altitude (velocity and direction) which allowed a full characterization of the turbulence in the upper atmosphere. This procedure was later adapted to the Generalized SCIDAR technique. This will be explained in detail in Chapter II.

For $\gamma$ Del, we have observed a rapid change of the turbulence profile with a time-scale of a few minutes only which shows the interest of a continuous turbulence monitoring to improve the performances of future adaptive optics systems in the case of very large telescopes or

| Turbulence parameters for the different layers | | | | | | |
|---|---|---|---|---|---|---|
| distance [km] | 19.6 | 18.8 | 17.1 | 13.7 | 13.1 | 9.4 |
| altitude [km] | 21.0 | 20.3 | 18.7 | 15.6 | 15.0 | 11.6 |
| wind velocity [m/s] | 14.5 | 14.5 | 6.9 | 28.6 | 38.1 | 46.9 |
| wind direction [degree] | 253 | 301 | 247 | 274 | 286 | 276 |
| $\tilde{J}$ amplitude | 2.2 | 3.0 | 11.2 | 3.0 | 5.0 | 10.7 |
| $V_j\tau$ [m] | .043 | .043 | .021 | .086 | .114 | .141 |
| $K$ attenuation | 0.86 | 0.85 | 0.95 | 0.59 | 0.45 | 0.33 |
| Corrected $\tilde{J}$ amplitude | 2.6 | 3.5 | 11.8 | 5.1 | 11.1 | 32.4 |

Table I.1: SCIDAR observations with PISCO: parameters of the optical turbulence for the 6 layers detected beyond a distance of 8 km for $\gamma$ Ari, during the first two minutes of observation. $\tilde{J}$ is in $10^{-15}$ [$m^{1/3}$].

interferometers.

The parameters derived from these observations were then used for simulations of astrometric uncertainties with a dual-field optical interferometer that will be described in Sect. I.4 (see also Daigne et al. (2000)). It will be shown that SCIDAR observations alone cannot allow the estimation of differential astrometric errors. Indeed SCIDAR measurements are not sensitive to turbulence scales larger than a few 0.1 m, whereas differential astrometry uncertainty is mainly dependent on the shape of turbulence spectra at much larger scales (a few 10 m). We proposed to complete remote investigation of atmospheric turbulence in altitude by performing simultaneous observations of differential angle-of-arrival between field stars.

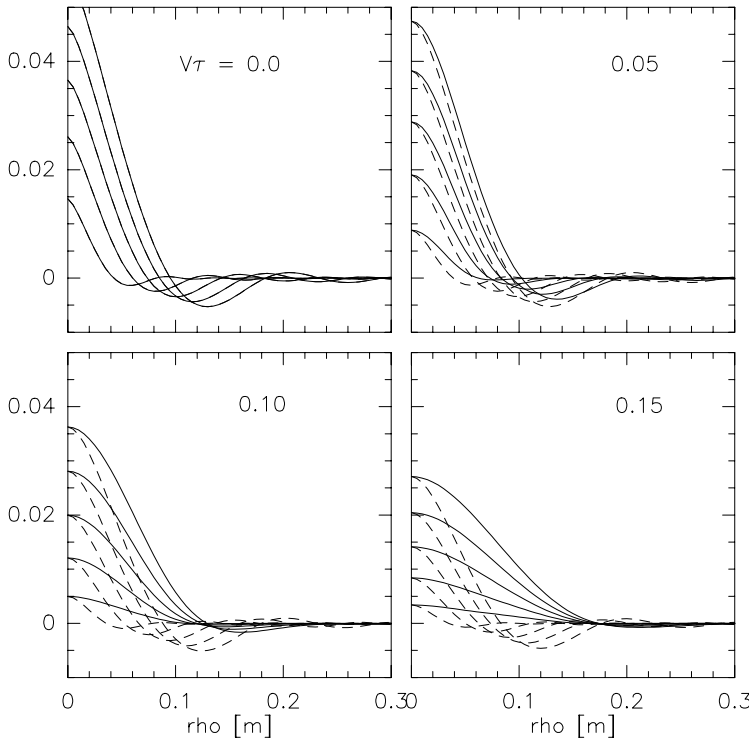


Figure I.8: Profile of the scintillation covariance function for turbulent layers at distances 5, 10, 15, 20 and 25 km. Solid line: profile along the direction of the wind, dashed line: in the perpendicular direction. The value of the product $V_j\tau$ [m] is indicated on each graph.

# I.4 Influence of the outer scale of turbulence on astrometric measurements

## I.4.1 Inner and outer scale of turbulence

The atmospheric turbulence is generally described by the Kolmogorov model. In fully developed turbulence, the kinetic energy of the large scale motions is transferred to smaller and smaller scale motions. This is known as a "cascade of energy", from large to small scale size. This cascade stops at small scale when the Reynolds number becomes small and the kinetic energy is dissipated into heat by viscous friction. The largest turbulent eddies have characteristic size $L_0$ called the *external scale* or *outer scale*, whereas the dissipation into heat happens for scale size $l_0$ called the *inner scale*. In the atmosphere, the outer and inner scales are typically some tens of meters and a few millimeters, respectively.

Within the inertial range, i.e., between $l_0$ and $L_0$, the kinetic energy is shown to be (by a dimensional reasoning only):

$$E(\kappa) \propto \kappa^{-5/3}$$

where $\kappa = \sqrt{\kappa_x^2 + \kappa_y^2 + \kappa_z^2}$. This is known as the *Kolmogorov law*. The corresponding 3D power spectrum of energy is given by:

$$\Phi_E(\overrightarrow{\kappa}) \propto \kappa^{-11/3}$$

Scalar quantities of the turbulent flow that are additive and passive (not affecting the dynamic of the medium) and conservative (not disappearing by chemical reaction) like the temperature $T$ and humidity $C$ also follow Kolmogorov law (Obukhov , 1949).

At optical wavelengths, the dependence of the fluctuations $N$ of the refractive index of air upon pressure $P$ and temperature $T$ is well approximated by the following formula derived from Gladstone law:

$$N = -77.6 \times 10^{-6} \frac{P}{T^2} \tilde{T}$$

where $\tilde{T}$ is the temperature fluctuations; $T$ and $\tilde{T}$ are in Kelvin, and $P$ in millibar. This equation shows that the refractive index fluctuations will also follow a Kolmogorov law. As a result, the power spectrum of the atmospheric air index fluctuations was modelled by Tatarskii (1961) as:

$$\Phi_N(\overrightarrow{\kappa}) = 0.033\, C_N^2\, \kappa^{-11/3}$$

Other models describe atmospheric turbulence on the whole spectrum, even outside the inertial domain. For instance, the empirical Von Kármán spectrum:

$$\Phi_N(\overrightarrow{\kappa}) = \frac{0.033\, C_N^2\, \exp -\kappa^2/\kappa_i^2}{\left[\kappa^2 + \kappa_0^2\right]^{11/6}} \qquad \text{where} \quad \kappa_0 = 2\pi/L_0 \quad \kappa_i = 5.91/l_0$$

This spectrum is plotted in Fig. I.9.

## I.4.2 Measurements of the outer scale of turbulence

Optical turbulence, produced high in the atmosphere, is the dominant factor limiting the astrometric precision of narrow-angle observations with a dual-field optical interferometer

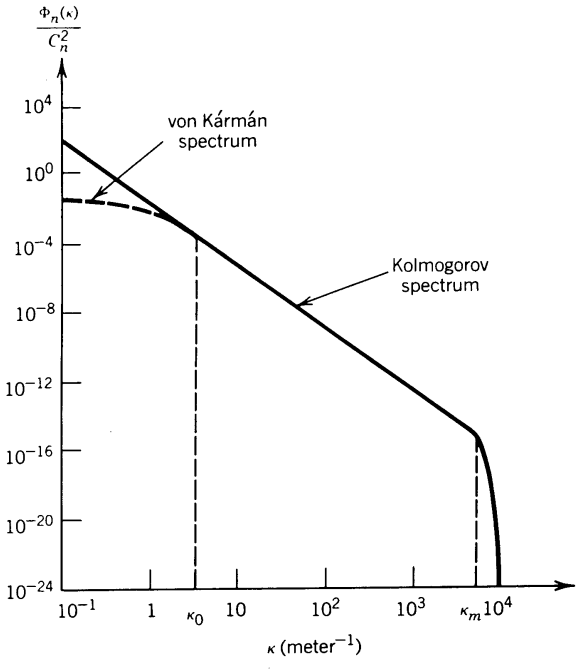


Figure I.9: Power spectrum of the atmospheric air index fluctuations (cf Goodman, 1985).

(Shao & Colavita, 1992; Colavita , 1994). Distribution profiles of turbulence can be obtained through SCIDAR measurements (for a review, see Avila (1998a) ). Wind velocity in the different turbulence layers can also be reached through cross-correlation of successive frames (Avila et al., 2001; Prieur et al., 2001), so that SCIDAR is a unique tool for diagnostics of optical turbulence and first evaluation of its effects in dual-field interferometry. But SCIDAR is mainly sensitive to short turbulence scale lengths, about a few centimeters, whereas astrometric measurements are sensitive to turbulence on much larger scale lengths, that is mostly dependent on a finite outer scale.

A dedicated instrument, the Generalized Seeing Monitor (GSM), has been developed for site testing and estimate, at ground level, of a spatial coherence outer scale $\mathcal{L}_0$ ( for a review, see Conan (2000) ). The basic principle is correlation of Angle-of-Arrival (AA) fluctuations measured by different small telescopes, in the observation of a single star. $\mathcal{L}_0$ is an average value of the (geo)physical outer scale $L_0(h)$ along the line of sight, weighted by the turbulence distribution, strong turbulence layers with a small $L_0$ value having a dominant effect (Borgnino , 1990).

In order to better probe layers in altitude, one has to reverse the GSM principle, for example by observing several field stars with a large ground telescope and measuring the corresponding AA fluctuations.

### I.4.3 Influence on astrometric interferometric measurements and Angle-of-Arrival fluctuations

In Daigne et al. (2000), we studied the influence of the outer scale of turbulence $L_0$ on the precision of angular measurements performed with a dual-field long baseline optical interferometer with some numerical simulations. We simulated both differential piston in dual-field

optical interferometry and differential AA mono-pupil observations. For those simulations, we used the optical turbulence and wind velocity parameters that we obtained from the "classical" SCIDAR experiment that was performed in 1998 with PISCO at Pic du Midi (Prieur et al., 2001). More precisely, we used the parameters of $\gamma$ Ari observations from TableI.1.

Simulations were performed for a 50m baseline interferometer, and telescope apertures of 1.5m diameter. The baseline was either parallel or perpendicular to the star separation. The separation angle was that of $\gamma$ Ari, i.e., 7.55". For AA simulations, with single-dish observations, the aperture was circular with 1.5m diameter, and the star separation was a variable, in the range 0 to 6 arcmin. Turbulence was supposed to be frozen in the medium, moving as a whole whatever the scale length, with a power spectrum given by a Von Kármán model (see Eq.I.4.1, with $L_0$ as a model parameter. Following Conan, Rousset , & Madec (1995), power spectra of differential AA and differential piston were obtained for each one of the turbulence layers (see Fig. I.10). Those spectra were used to derive the overall rms errors[1].

Differential piston rms is shown in Fig. I.11a, with different outer scale values. It is less than 0.16 $\mu$m, that is smaller than $\lambda$/10 in the $H$ and $K$ near-IR bands. The two stars are then in the same isoplanatic patch. For long exposures, the estimated rms differential piston depends mainly on the outer scale of turbulence, and not so much on baseline direction (except for large $L_0$ value). On power spectra of differential piston (Fig. I.10a-b), the third turbulence layer of Table I.1 has a dominant effect in the low frequency range.

Differential AA rms is shown on Fig. I.11b, for 3 sec. exposures. Its sensitivity to $L_0$ value increases with separation angle. But again, power spectra of differential AA (Fig. I.10c-d) show that dominant effects are due to the third (and slower) layer of turbulence, with quite a noticeable anisotropy, relative to the wind direction.

*Conclusions of this study*

On a particular situation, we have demonstrated the sensitivity of differential piston to outer scale of turbulence in a main turbulence layer at altitude, the one with the strongest SCIDAR signature. The $L_0$ value can be estimated through single dish differential AA measurements, provided the separation angle be large enough ($\geq$ 2 arcmin), and the exposure duration be optimized (about 3 seconds), depending on the wind velocity at altitude. With large enough apertures, the unique AA signature of turbulence layers at altitude should not be hidden by contributions from stronger optical turbulence in the first few kilometers above the telescope, so that a reverse GSM could be an operating principle for probing the outer scale of turbulence at altitude.

It thus appears that both AA and SCIDAR measurements can be performed with a single telescope whose aperture is about the size of the entrance pupil of an optical interferometer observing in the near-IR range ($D \simeq 1.5$ m). Those two techniques could thus be used on a telescope of the dual-field interferometer (DFI) during the observations, for determining the outer-scale, and for probing and tracking turbulence distribution and wind velocity.

[1] For each turbulent layer at altitude $h$, the noise power $\sigma^2_{N,h}$ is equal to the integral of the power spectral density $\Phi_{N,h}$

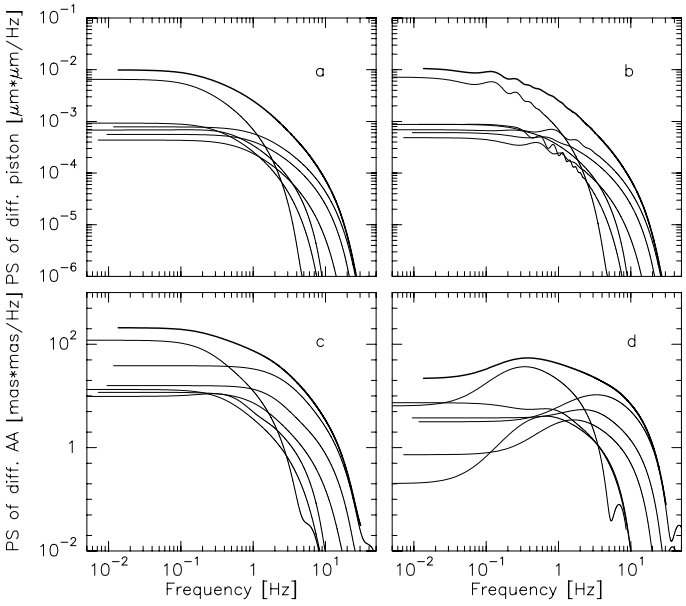


Figure I.10: a-b) Power spectrum of differential piston (interferometer) and c-d) Power spectrum of differential Angle-of-Arrival (mono-pupil) for each one of the turbulence layers, and for their summation (thick lines). a) and c) is along the star separation, and b) and d) is perpendicular to that direction, that is mainly along the wind direction. The outer scale of turbulence is 50 m. The star separation angle is 2' with single dish observations.

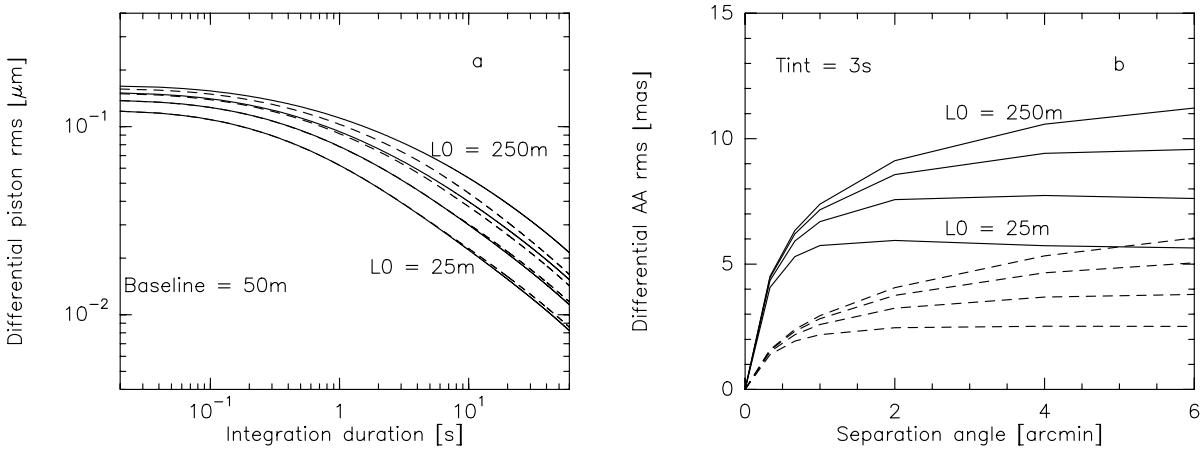


Figure I.11: Simulated measurement errors of a binary star for different values of the outer scale of turbulence ($L_0$ = 25, 50, 100 and 250 m). Top: differential piston error (case of a 50 m baseline dual-field interferometer). Bottom: differential Angle-of-Arrival error (case of a 1.5 m mono-pupil telescope). Two directions have been considered: along the star separation (full line), and perpendicular to it (dashed line). Figures from Daigne et al. (2000).

# Chapter II

# Automatic determination of wind profiles with Generalized SCIDAR

In Prieur et al. (2004), we presented an iterative method for deriving wind profiles from Generalized SCIDAR measurements, which can work in a non-supervised mode. It is an extension of our CLEAN-based method previously developed for $C_N^2$ profile determination for Pic du Midi observations with PISCO. The algorithm is based on a morphological analysis of the cross-correlation function of consecutive scintillation irradiance frames, with the introduction of some knowledge from the $C_N^2$ profiles, which are determined from the autocorrelation of those frames. This method was successfully tested on data from the site testing observations made at San Pedro Mártir in 2000 by R. Avila & J. Vernin, even on the most difficult cases.

## II.1 Introduction

The SCIDAR method (SCIntillation Detection And Ranging) was proposed by Rocca et al. (1974) to characterize the atmospheric turbulence that perturbs astronomical observations. This method is based on the analysis of the autocorrelation of irradiance images of a binary star, in the pupil plane. It allows the determination of (i) vertical profiles of the refractive-index structure $C_N^2(h)$, which characterizes the strength of the optical turbulence, and (ii) the velocities $\boldsymbol{V}$ of the turbulent layers[1].

The original (also called conventional) SCIDAR method did not allow the determination of the turbulence of layers located close to the ground level, or inside the dome. To allow such a determination, Fuchs et al. (1998) proposed to use defocused images and shift the (virtual) plane of analysis a few km below the pupil plane. Avila et al. (1997) implemented this method on a telescope. This extension of the SCIDAR method is known as Generalized SCIDAR, and will be noted GS in the following of this chapter

As this new method was very attractive, extensive GS observation campaigns were soon performed to study the turbulence above astronomical observatories (Avila et al., 1998; Klückers et al., 1998; Vernin et al., 2000,; Avila et al., 2004; Mckenna et al., 2003; Chun et al., 2002; García-Lorenzo, 2003). Although profiles of $C_N^2(h)$ are routinely calculated from those observations, with Maximum Entropy methods (Vernin, 1992; Klückers et al., 1998) or CLEAN

[1] In this chapter, two-dimensional vectors will be noted in bold

(Prieur et al., 2001), few papers presenting wind profiles had been published until our work on GS (Klückers et al., 1998; Avila et al., 2001; Vernin et al., 2000; Avila et al., 2004). The main reason is that wind parameters are rather difficult to retrieve from SCIDAR (or GS) data. To our knowledge, only very tedious interactive programs existed to do so (Avila et al., 2001). In this chapter we present the results of our investigations in order to perform an automatic determination of wind profiles that can be run in batch mode on a large amount of data. Some other details can be found in Prieur et al. (2004).

# II.2 Brief theory of (generalized)SCIDAR

The SCIDAR technique has been the subject of many papers (e.g. Rocca et al., 1974; Vernin & Azouit, 1983; Caccia et al., 1987; Avila et al., 1997, Klückers et al., 1998, Prieur et al., 2001). Here we only present the guidelines of conventional and generalized SCIDAR, in order to introduce the quantities useful for this chapter.

In this section we shall assume that the observations are performed at the zenith. For non-zero zenithal angles $\gamma$, the altitudes $h$ should be replaced by $h\cos^{-1}(\gamma)$ in all equations.

## II.2.1 Principle of the $C_{\rm N}^2(h)$ measurements

Let us first consider the observation of a single star in the presence of a single thin turbulent layer at altitude $h$ above the ground, with a thickness $\delta h$, and a refractive-index structure coefficient of $C_{\rm N}^2(h)$. This layer will introduce phase fluctuations in the light path that will generate intensity fluctuations, i.e., *scintillation*, at the level of the ground, whose covariance is $\mathcal{C}\left(\mathbf{r},h\right)\times C_{\rm N}^2(h)\delta h$. When assuming that the phase fluctuations produced by the layer have a Kolmogorov spectrum, it can be shown that:

$$\mathcal{C}\left(\mathbf{r},h\right)=0.66\pi^{1/3}\lambda^{-2}\int \mathrm{d}\mathbf{f}\ f^{-11/3}\sin^2\left(\pi\lambda h f^2\right)\exp(-2\mathrm{i}\pi\mathbf{f}\cdot\mathbf{r}), \tag{II.1}$$

where the symbol $\mathbf{f}$ represents the two-dimensional spatial frequency, and $f$ is its modulus. Hence the contribution $\sigma_I^2\left(h\right)$ of this layer to the total scintillation variance $\sigma_I^2$ at the ground level is given by:

$$\sigma_I^2\left(h\right)\equiv\mathcal{C}\left(0,h\right)\int_{h-\delta h/2}^{h+\delta h/2}C_{\rm N}^2(h)\mathrm{d}h=19.12\lambda^{-7/6}h^{5/6}\ J(h) \tag{II.2}$$

where $J(h)$ is the *optical turbulence factor* of this layer:

$$J(h)=\int_{h-\delta h/2}^{h+\delta h/2}C_{\rm N}^2(h)\mathrm{d}h \tag{II.3}$$

In the case of a double star whose components have an angular separation $\boldsymbol{\rho}$, the scintillation pattern will be duplicated at the level of the ground, with a horizontal distance $\boldsymbol{\rho}h$ between the two patterns. Hence, profiles of $C_{\rm N}^2(h)$ can be easily derived from the analysis of the mean spatial autocorrelation function of short exposure-time images of the scintillation pattern produced by a double star. This is the principle of the SCIDAR technique.

In original (or conventional) SCIDAR, the telescope pupil is imaged onto the detector, which makes the technique insensitive to turbulence close to the ground, because the scintillation variance is proportional to $h^{5/6}$ (cf. Eq. II.2). In GS, the plane of the detector is made the conjugate of a plane at a distance $h_{\rm gs}$ (the analysis plane), which lies a few kilometers below the telescope pupil (i.e. $h_{\rm gs} < 0$). In this case the turbulence near the ground, including that in the telescope dome, becomes detectable because the distance relevant for scintillation produced by a turbulent layer at an altitude $h$ is now:

$$H = h - h_{\rm gs} \tag{II.4}$$

which is indeed the distance between the phase screen, and the plane of observation (cf Fig. II.1). Therefore, Eqs. II.1 and II.2 remain valid when simply replacing $h$ by $H$.

As the different turbulent layers are statistically independent, the contribution of each one is added, and the total theoretical GS autocorrelation function can be written as (cf. Roddier, 1981):

$$C^{**}_{\rm gs}\left(\mathbf{r}\right) = \int_{-h_{\rm gs}}^{+\infty} {\rm d}h\; C^2_{\rm N}(h)\left[\, a\,\mathcal{C}\left(\mathbf{r},H\right) + b\,\mathcal{C}\left(\mathbf{r}-\boldsymbol{\rho}H,H\right) + b\,\mathcal{C}\left(\mathbf{r}+\boldsymbol{\rho}H,H\right)\,\right] \tag{II.5}$$

The factors $a$ and $b$ of Eq. (II.5) are given by

$$a = \frac{1+\alpha^2}{\left(1+\alpha\right)^2} \quad \text{and} \quad b = \frac{\alpha}{\left(1+\alpha\right)^2}, \quad \text{with} \quad \alpha = 10^{-0.4\Delta m}, \tag{II.6}$$

where $\Delta m$ is the magnitude difference of the double star.

Hence, all the information needed to retrieve $C^2_{\rm N}(h)$ is contained in a radial section of $C^{**}_{\rm gs}\left(\mathbf{r}\right)$ along the double star separation. Furthermore, it is convenient to isolate the satellites from the central peak, because in the latter the contribution of each layer is indistinguishable from that of the others, as they are added, and it contains the uncorrelated noise. The result of the radial section ($x$ direction) and of the isolation of say the peak on the left hand side located at $x_{left}$, for experimental data, can be expressed as:

$$B^{**}_{\rm gs}\left(x\right) = \int_{-h_{\rm gs}}^{+\infty} {\rm d}h\; K\left(x - x_{left}, H\right)\; C^2_{\rm N}(h) + N(x). \tag{II.7}$$

$N(x)$ is the noise, and the kernel $K\left(x - x_{left}, H\right)$ is a radial section of $b\,\mathcal{C}\left(\mathbf{r}-\boldsymbol{\rho}H,H\right) * S\left(\mathbf{r}\right)$, where $S\left(\mathbf{r}\right)$ is the autocorrelation of the impulse response (PSF) of the detector. The determination of $C^2_{\rm N}\left(h\right)$ is thus an inverse problem, obeying Eq. (II.7), which is an equation of Fredholm type. We have seen in Sect. I.3 that this problem could be solved by various numerical methods, for instance using a maximum entropy algorithm (e.g., Vernin, 1992) or CLEAN (Prieur et al., 2001).

Vernin & Azouit (1983) showed that $\Delta\mathcal{R}(h)$ the equivalent radius (width at half maximum) of a correlation peak for a given layer at altitude $h$ is proportional to $\sqrt{\lambda(h-h_{\rm gs})}$. In (Prieur et al., 2001) (see also Sect. I.2.1), we determined the proportionality constant to be equal to 0.78, so that:

$$\Delta\mathcal{R}(h) = 0.78\sqrt{\lambda(h-h_{\rm gs})}. \tag{II.8}$$

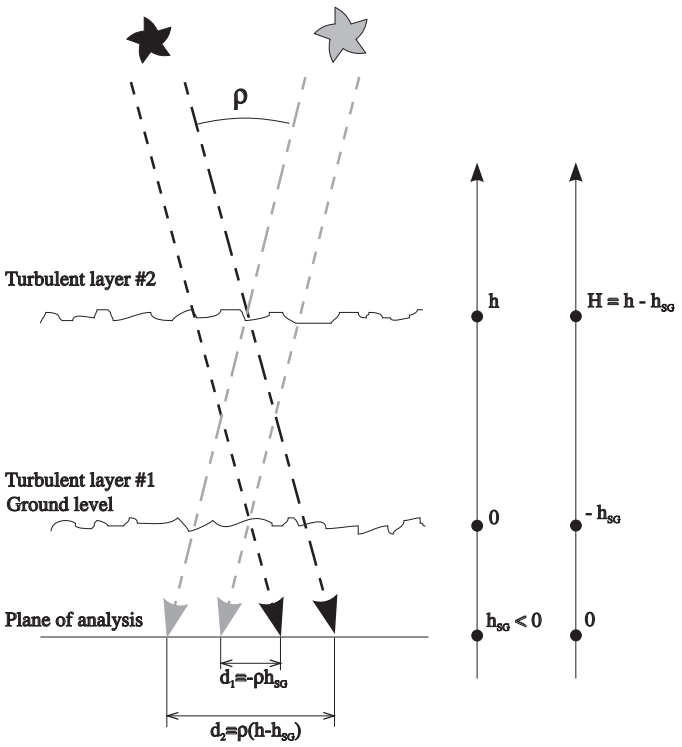


Figure II.1: Principle of the generalized SCIDAR.

### II.2.2 Principle of wind velocity $\mathbf{V}(h)$ measurements

In the following, we shall assume that the turbulent structures are carried by the mean wind without deformation. This assumption is known as *Taylor hypothesis* or *frozen turbulence*, and is valid for short enough time intervals. In this case, the scintillation pattern produced by a layer at altitude $h$, where the mean (horizontal) wind velocity is $\mathbf{V}(h)$, moves on the analysis plane a distance $\mathbf{V}(h)\,\Delta t$ in a time $\Delta t$. Hence, $\mathbf{V}(h)$ can be determined by analyzing the cross-correlation of pairs of scintillation images taken at times separated by $\Delta t$. As in the case of the autocorrelation (cf. Sect II.2.1), the presence of a turbulent layer at height $H$ produces a triplet in the cross-correlation function, with a separation of $\pm\boldsymbol{\rho}H$ between the central peak and the satellites. But here the central peak is no longer situated at the origin: it is located at the point $\mathbf{r} = \mathbf{V}(h)\,\Delta t$. In the case of multiple layers, by analogy with Eq. (II.5), the cross-correlation can be written as:

$$C_{\mathrm{c}}^{**}(\mathbf{r},\Delta t) = \int_{-h_{\mathrm{gs}}}^{+\infty} \mathrm{d}h\; C_{\mathrm{N}}^{2}(h)\,[\; a\,\mathcal{C}_{\mathrm{c}}(\mathbf{r}-\mathbf{V}(h)\Delta t, H) + b\,\mathcal{C}_{\mathrm{c}}(\mathbf{r}-\mathbf{V}(h)\Delta t-\boldsymbol{\rho}H, H) + b\,\mathcal{C}_{\mathrm{c}}(\mathbf{r}-\mathbf{V}(h)\Delta t+\boldsymbol{\rho}H, H)\;]\,. \tag{II.9}$$

$\mathcal{C}_{\mathrm{c}}$ differs slightly from $\mathcal{C}$ (Eq. II.5) because of a certain amount of temporal de-correlation of the scintillation (partial failure of the Taylor hypothesis), and a possible fluctuation of $\mathbf{V}(h)$ during the integration time. Those two effects reduce the amplitude of the scintillation covariance and widen it, respectively (Caccia et al., 1987). In the current implementation of our method we have assumed that $\mathcal{C}_{\mathrm{c}}(\mathbf{r},H) \propto \mathcal{C}(\mathbf{r},H)$ and neglected the (small) width

increase. The absence of artifacts in the residual maps we have obtained so far indicates that this assumption was valid for the data we have processed with our method.

### II.2.3 Sensitivity of the method

Experimentally, we are limited to a finite pupil size, and the intensity of $B^{**}_{\rm gs}(x)$ of Eq. II.7 is modulated (i.e., multiplied) by $P(x)$, the autocorrelation of the pupil. We can thus expect that the noise increases with $x$, the abscissa of the secondary peak. As can be seen in Fig. II.1, this quantity is proportional to $\boldsymbol{\rho}$, the angular separation of the binary and to $h_{GS}$, the distance of the analysis plane from the ground level. Hence for GS observations, one should select binaries appropriately to obtain a good compromise between large values of $x$ to allow a good separation of turbulent layers with a high resolution in altitude, and small values of $x$ to reduce the noise.

When neglecting the read-out noise, Tokovinin (1997) has shown that the statistical rms noise of $B^{**}_{\rm gs}(x)$ per frame is given by:

$$\Delta B^{**}_{\rm gs}(x) = \left(a\,\sigma_I^2 + 1/N_{\rm ph}\right)/\sqrt{M(x)}, \tag{II.10}$$

where $N_{\rm ph}$ is the mean number of photons per coherence area of the scintillation pattern (radius $r_c$) and $M(x)$ is the number of independent cells, i.e., the ratio of $P(x)$, the overlapping pupil area, to $\pi r_c^2$ the coherence area of the scintillation patterns. Following Vernin & Azouit (1983), we take $r_c$ equal to the Fresnel radius of the turbulent layer which dominates the scintillation pattern (i.e., with the largest $\sigma_I^2(h)$). We then have $r_c = \sqrt{\lambda H_0/2\pi}$, by noting $H_0$, the distance of that layer to the plane of analysis, and:

$$M(x) = 2P(x)/(\lambda H_0) \tag{II.11}$$

When considering Eq. II.7 at $x_{left}$, the center of the left satellite, we can estimate the uncertainty of the optical turbulence factor (cf. Eq. II.3):

$$\Delta J(x_{left}) = \frac{\Delta B^{**}_{\rm gs}(x_{left})}{K(0,H)} \tag{II.12}$$

with $K(0,H) = b\,\mathcal{C}(0,H) * S(0)$. Using Eqs. II.2, II.10 and II.11, it comes:

$$\Delta J(x_{left}) = \frac{3.70\,10^{-2}\,\lambda^{5/3} H^{-5/6} H_0^{1/2}\,(a\,\sigma_I^2 + 1/N_{\rm ph})}{b\,\sqrt{P(x)}} \tag{II.13}$$

This noise can be reduced by averaging the signal on $n$ independent frames and integrating it over the full area of the satellites. More generally, the total noise on the estimation of $J$ for given layer from the measurement of a triplet can then be approximated with:

$$N_J(H) \approx \frac{\Delta J(x_{left})}{c_\tau\,\sqrt{n}\,\sqrt{H/H_0}} \tag{II.14}$$

where $c_\tau$ is the attenuation factor affecting the signal of various origin such as the decorrelation due to the length of the integration time, the non-steadiness of the atmospheric turbulence and the deviations from Taylor's assumption. We have found experimentally that a typical value of $c_\tau$ is $\sim 0.7$. The term $\sqrt{H/H_0}$ takes into account the reduction of noise due to the possible integration of the signal on a disk of diameter $\Delta\mathcal{R}(h)$ (cf. Eq. II.8).

# II.3 Automatic wind velocity measurements

## II.3.1 Introduction

From the previous section, we see that the basic problem to obtain wind velocity profiles from the cross-correlation function $C_c^{**}$ is to detect the triplets produced by the turbulent layers. For each triplet, the wind parameters (horizontal amplitude and direction) can be derived from the position of the central peak, whereas the altitude of the layer are computed from the distance between the two satellites.

The experimental data to process consists of images which are measurements of the 2-D spatio-temporal cross-correlation function $C_c^{**}(\mathbf{r}, \Delta t)$ (with $\Delta t = 20$ ms or 40 ms). In the following we shall assume that they have been filtered out from experimental noise and rotated so that the lines ($x$ axis, in the following) are parallel to the direction of separation of the binary, as those assumptions were true for the cross-correlation data that we have used to test our method.

## II.3.2 Principle of our method

We have chosen to use an iterative approach based on the CLEAN algorithm, as we did for the inversion of $C_N^2$ profiles for SCIDAR measurements (Prieur et al., 2001). We wanted to take advantage of the experience acquired with the interactive program developed by Avila et al. (2001), which had shown its efficiency in providing good measurements. With Avila's program, the peaks are removed from the cross-correlation function with successive steps. For each step, the location of the central peak and satellites of a triplet are entered by the user, with the mouse, and then removed from the cross-correlation function. The user performs as many iterations as necessary in order to obtain a final image without any detectable peaks.

The method we propose is an "automated version" of Avila's program. For each iteration, the image is scanned for searching a central peak and two satellites. The validity of this triplet is determined with an analysis of the morphology, the brightness of the peaks, and the scintillation variance expected at the corresponding altitude. When all criteria are satisfied, the parameters of this layer (altitude, wind velocity, and direction) are stored into a file, and this triplet is removed (i.e. "cleaned"). The resulting image will be called *residual map*, whereas the image built with the valid triplets will be called *clean map*. The program proceeds with successive iterations, in order to detect (and then remove) all the triplets that are associated with turbulent layers.

## II.3.3 Description of the algorithm

Let's define the main objects that we shall use in this section. The `cpeaks` and the `clusters`, are associated with the central peaks and the satellites, respectively. The `triplets` are made of two `clusters` and one `cpeak`. The `cclean` will be the CLEAN components detected in the CLEAN process. In our current implementation in C, they are represented as "structures", with many fields to qualify them (position, intensity, size, etc). In object-oriented languages, they could be genuine "objects".

The algorithm is presented in Fig. II.2. It proceeds in four steps:

**Step 1: Detection of the central peak**

We first determine the center of the central peak `cpeak` by looking for the maximum in the current residual map (which is initialized to the cross-correlation function when starting the program). Its intensity will be called `cpeak.zcent`. A Gaussian function is then fitted within a small region around that maximum, which allows a more precise determination of the location (`cpeak.xcent, cpeak.ycent`) of the center of `cpeak`, and thus of the velocity of the possible corresponding turbulent layer(s).

To allow for subsequent detection of the (fainter) satellites, the intensity of `cpeak` needs to be large enough. We use a threshold on `cpeak.zcent` of `xsigma1` for validating this peak. A typical value for `xsigma1` is $6\,\sigma_c$, where $\sigma_c$ was the standard deviation of the background (i.e. area free of any triplets) of the cross-correlation function. The program stops when the residual map does not exhibit any maxima larger than this value.

**Step 2: Detection of CLEAN components (satellites)**

Then an iterative CLEAN process of the satellites is performed inside the horizontal strip centered on (`cpeak.xcent, cpeak.ycent`), with a width $\Delta\mathcal{R}$ (cf. Eq. II.8). For each $j$th iteration, the location of the pixel with the maximum intensity is searched for. Its coordinates are noted (`cclean[j].x, cclean[j].y`), and its intensity `cclean[j].z`. Then the function $\alpha \times \mathcal{C}\left(\mathbf{r}, H\right) * S(\mathbf{r})$ centered on (`cclean[j].x, cclean[j].y`), is subtracted from the current residual map to "clean" this central peak (cf. Sect II.2). Like in most implementations of the CLEAN method, only a fraction of the maximum is "cleaned" at each iteration (we use $\alpha = 0.30$). The value of $H$, which is needed to compute $\mathcal{C}\left(\mathbf{r}, H\right)$ is derived from the distance from `cclean[j]` to `cpeak` (cf. Sect. II.2). The iterative process on $j$ stops when the noise level is reached, i.e. `cclean[j].z` $<$ `xsigma2`, or when the number of CLEAN components exceeds a certain limit `j_max`. A typical value for `xsigma2` is $3\,\sigma_c$. The test on `j_max` is needed for safety to avoid problems when `xsigma2` has been set too small.

**Step 3: Gathering CLEAN components into `triplets`**

A morphological analysis is then performed on the set of the CLEAN components `cclean[j]` detected in step 2. The purpose of this analysis is to sort out those numerous components and select those who belong to possible satellites associated with the central peak `cpeak`. This is done in two steps:

- The routine `group_to_clusters` groups the components `cclean[j]` into `clusters`, that will be candidates for satellites associated with turbulent layers, by performing a morphological analysis. This routine proceeds with successive iterations. First, the density of neighbours within $\mathcal{R}(h)$ (Eq. II.8) is computed for each CLEAN component. The component having the maximum density of neighbours is taken as the center of a new cluster, and its neighbours (within $\mathcal{R}(h)$) are associated with this cluster. The components belonging to this cluster are then neutralized for the next iterations. The routine stops when the maximum neighbour density is too small (typically less than 3).

- The routine `make_triplets` performs an analysis of those clusters in order to select the pairs of clusters that will be good candidates for satellites of `cpeak` linked to a

turbulent layer. When such a pair is found it constitutes a `triplet`. The criteria used here are morphological only: two clusters located on the left and on the right of the central peak `cpeak`, respectively, form a new `triplet` when their distances to that peak are similar. At this stage, it is also possible to detect some "foreign peaks", i.e. possible central peaks (and their satellites) generated by turbulent layers that have different velocities from that of the layer(s) associated with the central peak `cpeak` (see examples in Sect. II.4.1). Indeed, a foreign central peak can be characterized as a bright cluster without any counterpart on the other side (left/right) relative to the central peak `cpeak`, with some satellites located symmetrically relative to it. Foreign peaks with their corresponding satellites are then processed separately.

At the end of this analysis, all the components `cclean[j]` that do not belong to clusters that have been grouped into `triplets` are removed from the CLEAN map, and the residual map is updated accordingly.

**Step 4: Testing the validity of the `triplets`**

Two tests of validity are then performed for each `triplet`: (loop on `it` index in Fig. II.2).

- `check_symmetry`: a thorough analysis of the symmetry of the two clusters belonging to the `triplet` relative to the central peak is performed. For the morphology, we check that the variances in $x$ and $y$ of the left/right distributions of the `cclean` components are similar, and that the mean values for $y$ on both sides are also similar. Concerning the intensities, both clusters should have a comparable number of `cclean` components, and the intensity of the central peak should be larger than that of the satellites (cf. Sect. II.2). Here the main difficulty is a possible contamination by a foreign peak which would have not been detected by the routine `make_triplet`.

- `check_altitude`: a final test of the validity of the clusters is done using the $C_{\mathrm{N}}^2$ profile. The selected clusters should correspond to an altitude $H$ where the scintillation variance, $\sigma_I^2(H)$, is larger than the threshold `xsigma2` used for detecting the satellites in the cross-correlation function. Note that the profile of the scintillation variance is derived from the $C_{\mathrm{N}}^2$ profile using Eq. II.2.

In the case of "multiple layers", i.e. turbulence layers with similar wind velocities and different altitudes, two or more `triplets` are associated with the central peak `cpeak`, and the layer index `klayer` is increased accordingly. Actually, in the current implementation of this program, a more precise determination of the location of the central peak is performed for each valid `triplet`, taking into account the location of the two satellites. This allow us to disentangle the cases when multiple layers have their central peaks superimposed.

Each time a valid triplet is found, the central peak is "cleaned" using the information contained in the satellites. The program removes from that peak $\frac{a\,\alpha}{b}\,\mathcal{C}\,(\mathbf{r}, H) * S(\mathbf{r})$ (see Eqs. II.1 and II.6). At the end of the process, there may remain some non-negligible residuals at this location, since the satellites are not always fully detected, due to the presence of noise. Thus, to allow the algorithm to converge, all pixels belonging to the disk centered on (`cpeak.xcent, cpeak.ycent`) with a diameter $\Delta\mathcal{R}$ are invalidated for further search of central peaks in the residual map.

When a `triplet` is rejected during this analysis, all CLEAN components belonging to its two `clusters` are removed from the CLEAN map, and the residual map is updated accordingly.

**General remarks:**

Note that all the CLEAN components that are not associated with satellites of valid `triplets` are restored to the residual map. They are thus available for another processing in subsequent iterations. This allows successful analysis of complex cases (e.g., examples of Sect. II.4.1).

The sensitivity of the algorithm can be easily tuned by changing the values of the two thresholds `xsigma1` and `xsigma2` that are used to stop the search for the central peak and the satellites, respectively.

An option for processing structures with a single satellite is also possible. This may be needed when the binary star is widely separated and/or when the wind velocities are large: one of the satellites may fall out of the cross-correlation map. In this case, the tests about symmetry are invalidated, and the only remaining test is that performed by `check_altitude` with the $\sigma_I^2$ profile. To improve the stability, and avoid a possible avalanche of spurious detections, the thresholds `xsigma1` and `xsigma2` may then need to be enlarged, i.e. the central peak and its satellite must have a better signal-to-noise ratio than when full triplets are detected.

# II.4 Analysis of the results

## II.4.1 Examples of processing

We present here some examples to illustrate the processing by our program of some typical cases.

**Multiple layers**

The detection of layers with similar velocities is rather difficult because the corresponding central peaks are superimposed. The triplets 1 and 2 of Fig.II.4.A illustrate this case. Moreover, the left satellite of triplet 1 is mixed with the central peak of triplet 5. Despite those two difficulties, the program identified well each layer. It is an example of "multiple layers" (cf. Step 4 of Sect. II.3.3). The pairs of clusters corresponding to the two layers 1 and 2 located at different altitudes are grouped to the same central peak to form two triplets. After validation of those triplets, the accurate location of the central peaks is then set to the mean of the corresponding satellites centers.

**Thick layer**

Rather often, the data show comma-like structures, which correspond to a series of layers at similar altitudes (a so-called "thick layer") and significantly different velocities. An example is presented in Fig. II.4.Bb. The program finds four layers in the "comma" structure on the bottom-left corner of the cross-correlation maps. As can be seen in Fig. II.4.Ba layers 3, 5 and 6 are located at the same altitude whereas layer 4 is slightly higher. Indeed when the altitude differences are smaller than the GS altitude resolution $\Delta\mathcal{R}(h)/\boldsymbol{\rho}$ (cf. Eq. II.8), the same (mean) altitude is attributed to those layers.

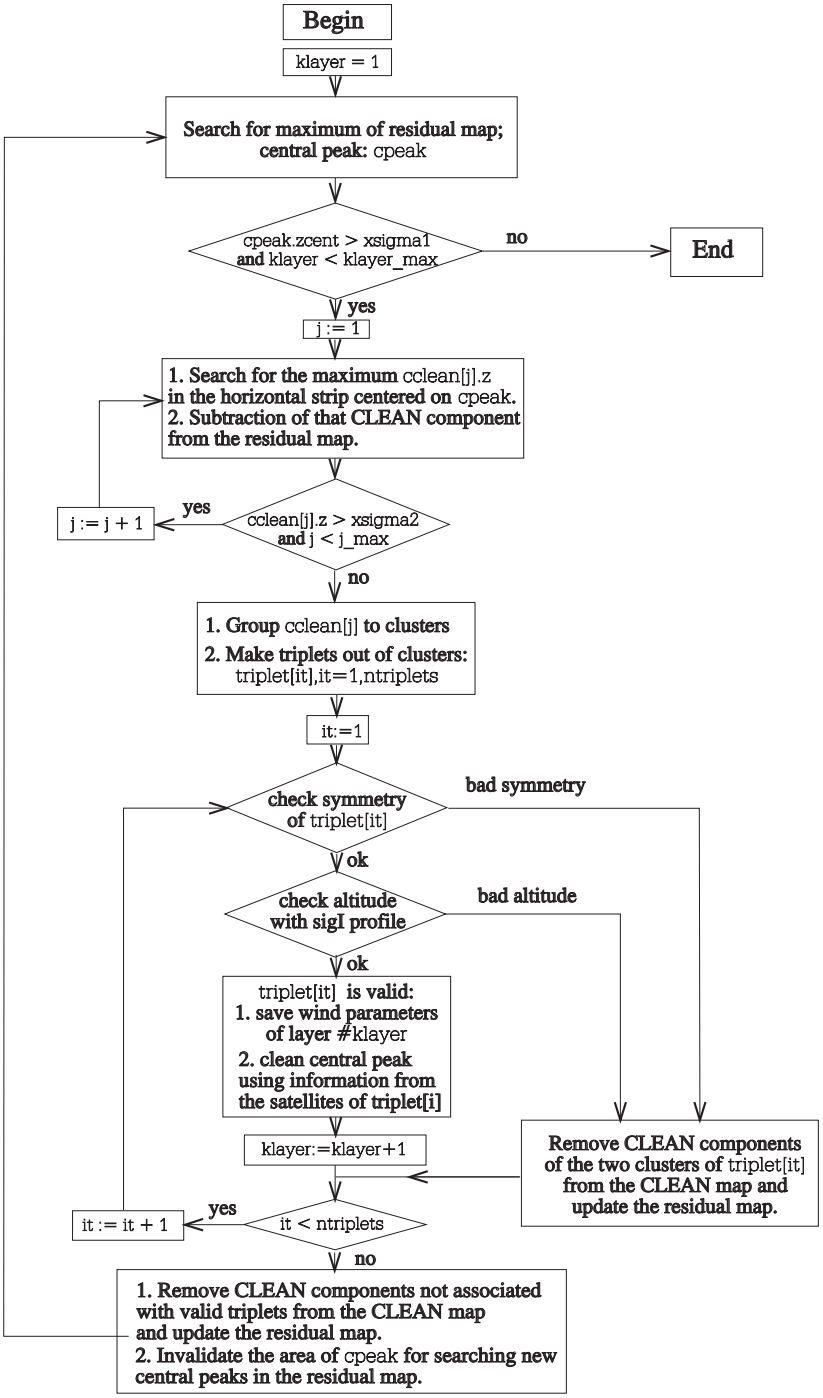


Figure II.2: Algorithm of our method for computing wind profiles.

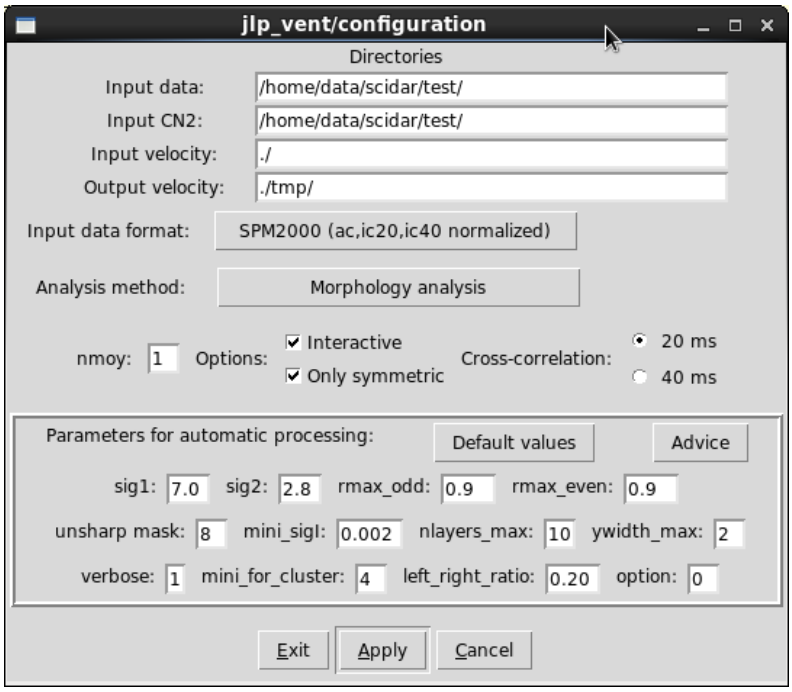


Figure II.3: Control panel used for starting the processing of generalized SCIDAR data by our wind vertical profile inversion program.

### Mixed-up case

Figs. II.4.Cb illustrates the case of a particularly difficult situation when triplets are mixed up along the same line (here the triplets 2 and 3). This figure shows that the program is able to handle such situations. As explained in Sect. II.3.3, this can be done in two ways: either by identifying a "foreign" central peak and its satellites during the processing of the brightest (and first detected) central peak, or by rejecting all the clusters not associated with the brightest central peak during this processing and by a specific processing of the "foreign" triplet during the subsequent iteration which starts by the detection of the central foreign peak.

### Wind velocity at the ground level

When the separation of the double star and/or the analysis-plane distance from the pupil ($h_{\rm gs}$) are not large enough, the turbulence near the ground can produce triplets with satellites partially superimposed on the central peak.

This is the case of layers 1 and 2 in Fig. II.4.Bb and layer 1 in Fig. II.4.Cb. As can be seen, the program handles well this complexity. For altitudes close to the ground level, the program works with the concept of "pattern recognition". The clusters corresponding to the satellites are identified by a thorough analysis of the intensity profile around the central peak.

The detection of the wind at the level of the ground is a very important feature because it enables us to determine the $C_{\rm N}^2$ inside the telescope dome. As explained by Avila et al. (2001), when two layers are detected at ground level with zero and non-zero velocities, respectively, then the first layer can be attributed to the turbulence inside the dome.

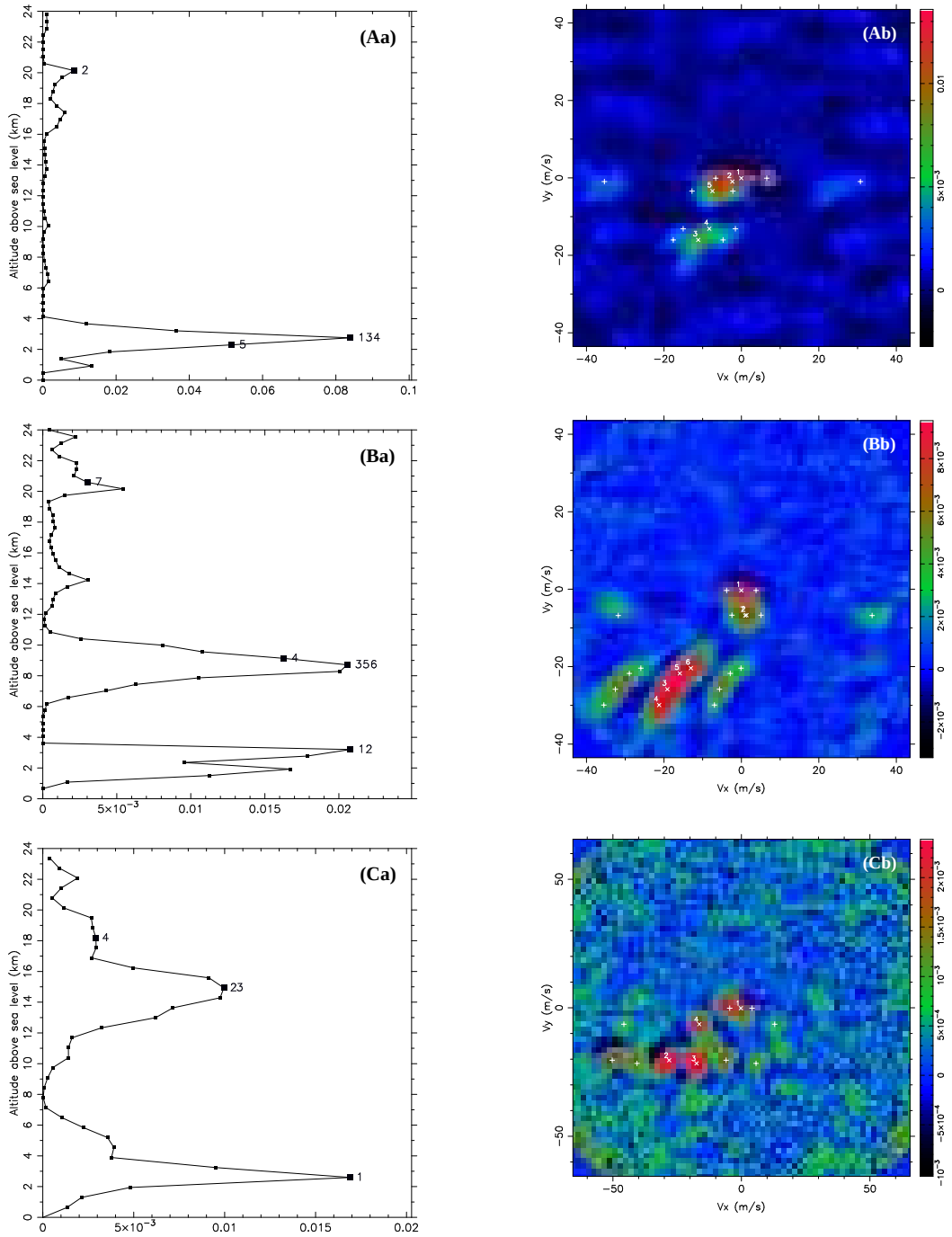


Figure II.4: Examples of automatic processing. From top to bottom: A. multiple layers with similar velocities; B. thick layer with a velocity gradient; C. superimposed triplets. Left (a): Scintillation variance profile. Right (b): cross-correlation function with crosses on the detected peaks: "$\times$" for central peaks, and "$+$" for satellites.

### II.4.2 Comparison with interactive processing

In this section, we compare the results derived with this method to those obtained by R. Avila with the "interactive" data reduction. We have used the campaign of GS observations performed in 2000 with the 2.1 m telescope of San Pedro Mártir (SPM), which are described in Avila et al. (2004).

In Figs II.5a and II.5b, we have displayed the velocity profiles obtained for the night of May 19th 2000 with the automatic and interactive programs, respectively. In this example, a good compromise between sensitivity and robustness was obtained with `xsigma1` $\sim 7$ and `xsigma2` $\sim 2.4$. For each observation, we have plotted a black dot at altitude zero, when the turbulence inside the dome (with zero velocity) was detected. It thus clearly appears that our program detects very well the turbulence layers close to the level of the ground, and even inside the dome. Furthermore, the detection rates in automatic and interactive modes are very similar.

The $C_N^2$ profiles measured during that night are displayed in Fig. II.5c. This night can be considered as typical with the highest velocity winds of around 30 m.s$^{-1}$ for the turbulent layers at high altitude in the range 10–15 km. In this plot, the altitude of 2800 m of SPM observatory is indicated with a white line.

Figs II.5a and II.5b show that the results obtained by the interactive and automatic modes are in very good agreement, especially for the altitudes with a $C_N^2$ with a good signal-to-noise ratio. Indeed, on the files we have processed, the main differences between the two modes were found for the altitudes with a small level of turbulence, which correspond to a small signal-to-noise ratio (SNR) of the $C_N^2$ profiles. But there also remains some particularly difficult situations with significant differences between interactive and automatic procedures although the SNR is good. The program (and humans) may not detect all the layers and/or give false detections. This rate of false detection is dependent on the complexity of the situations and on the values of `xsigma1` and `xsigma2`, which tune the sensitivity.

Of course this program is not perfect. Despite all our efforts, it cannot integrate all the wisdom of human brain. There will always remain some situations when a skilled user will be superior to this program, and will detect some turbulent layers with a lower SNR or better disentangle particularly complex cases. The CLEAN-based process we have chosen is versatile, and allows a full integration of the automatic and the interactive modes. In the current version of our program, the user can add or remove triplets interactively on the results obtained with the automatic mode. For desperate cases, the user can even process everything in the interactive mode only.

We can quantify the level of detection with the *filling factor*, which is defined as the ratio of the sum of $J(h)$ for the detected layers over the total sum of $J(h)$ for all layers. In Fig. II.6a, we have displayed the filling factor versus the time of observation for the measurements of the 19th May. In this figure, one can see that the automatic and interactive procedure lead to very similar filling factors, which indicates that the detection levels are nearly the same in both cases. The parameters that can be derived from the two sets of measurements are also very similar.

Fig. II.6b shows an example of $\tau_{\rm AO}$, the coherence time for full-correction adaptive optics, derived from the turbulence and wind velocity using (Roddier, Gilli, & Lund, 1982):

$$\tau_{\rm AO} = 0.519 \left(\frac{2\pi}{\lambda}\right)^{-6/5} \left[\int {\rm d}h \, |\mathbf{V}(h)|^{5/3} \, C_{\rm N}^2(h)\right]^{-3/5} \qquad \text{(II.15)}$$

The performances of both the interactive and automatic procedures can also be compared with the theoretical expectations using the noise estimation provided by Eq. II.14. In Fig. II.7, we have displayed the $J$ amplitudes of the detected layers and the theoretical curves corresponding to SNR=3 for the two binaries $\zeta$ Crb and 95 Her observed during the night of May 19th 2000 (with $h_{\rm gs} = -4$ km, $\sigma_I^2 \sim 0.34$, $n = 2000$, $H_0 = 13$ km, and $N_{\rm ph} \sim 100$ and 120 photons for $\zeta$ Crb and 95 Her, respectively). This figure shows that the detectivities of the automatic and interactive procedures are very similar, and are close to the 3-$\sigma$ level.

## II.5 Conclusion

Our CLEAN-based method was implemented and successfully tested on extensive data from GS observations made in San Pedro Mártir in 2000. The wind velocity parameters (velocity and direction) derived with this method are fully compatible with the results obtained with interactive programs.

This method allows an automatic determination of the wind parameters in altitude, which, combined with the $C_{\rm N}^2$ profiles, provides a full characterization of the turbulence above the site of observation. in a non-supervised mode. This opens the possibility of processing large amounts of data, and even doing real-time processing. Adaptive optics systems working on telescopes located on the same site could then take advantage of the knowledge of the turbulence parameters for a better efficiency.

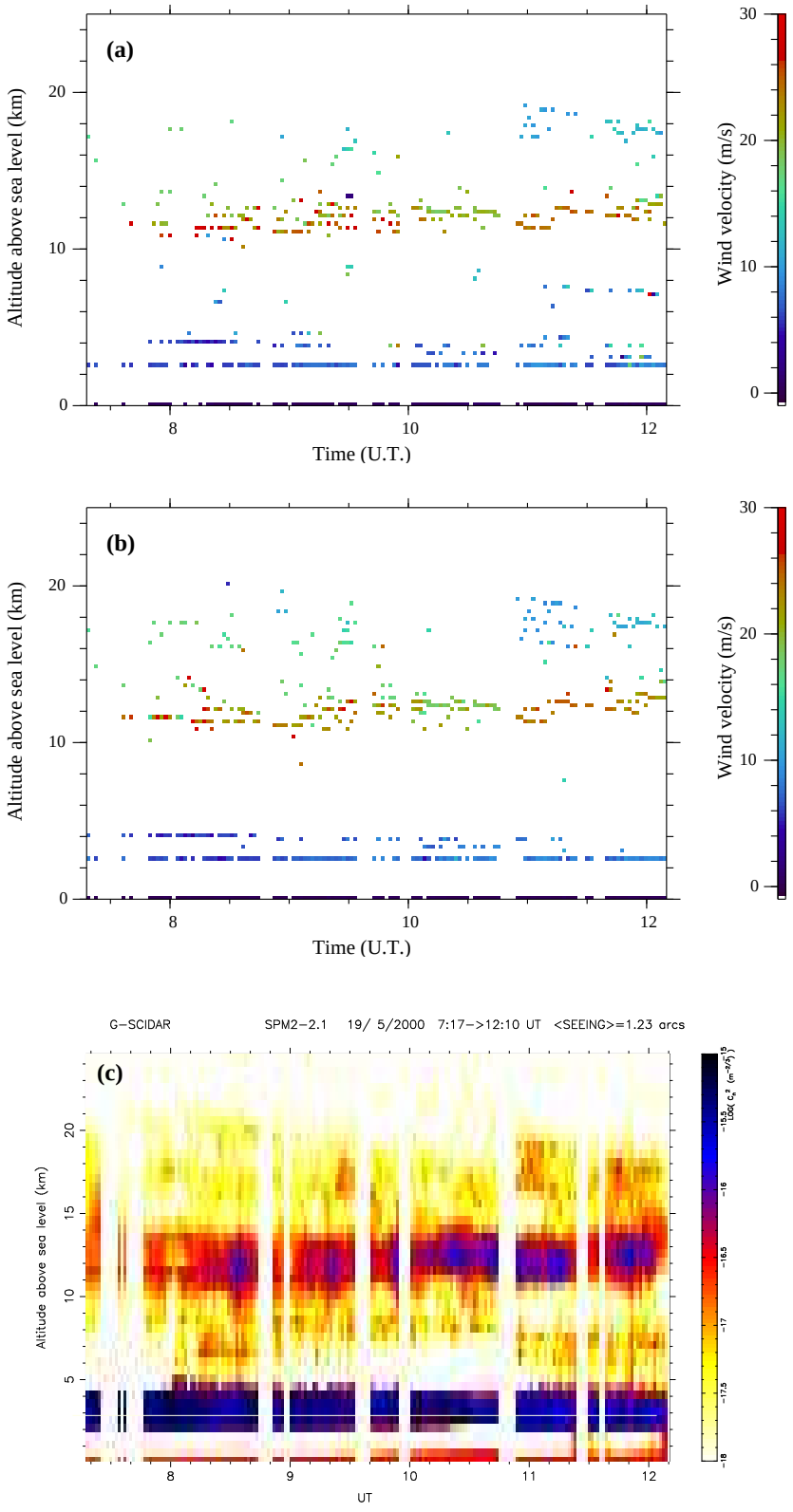


Figure II.5: Vertical wind velocity profiles measured with automatic (a), and interactive (b) procedures. The corresponding $C_N^2$ profile is displayed in (c) (night of 19/05/2000).

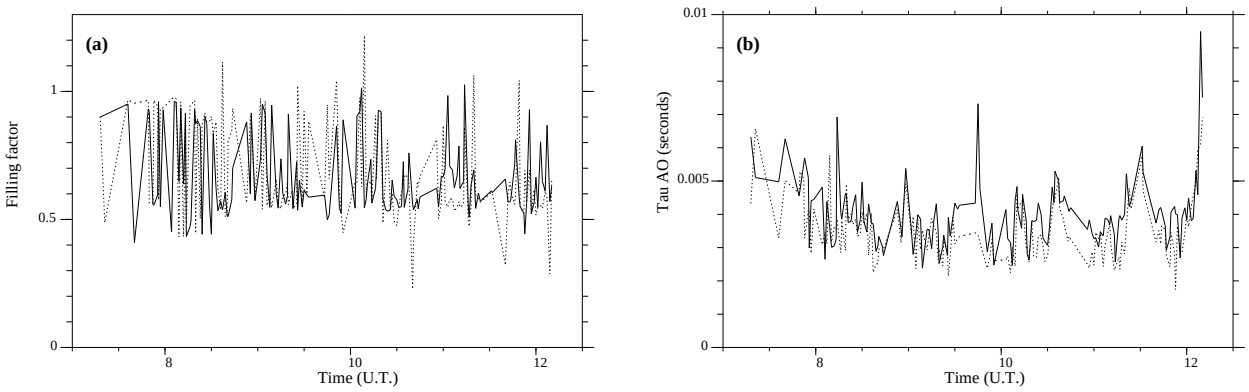


Figure II.6: Filling factor (a), and $\tau_{\rm AO}$ (coherence time for full correction Adaptive Optics) (b) obtained with automatic (solid line) and interactive (dashed line) procedures, versus the time of observation (night of 19/05/2000).

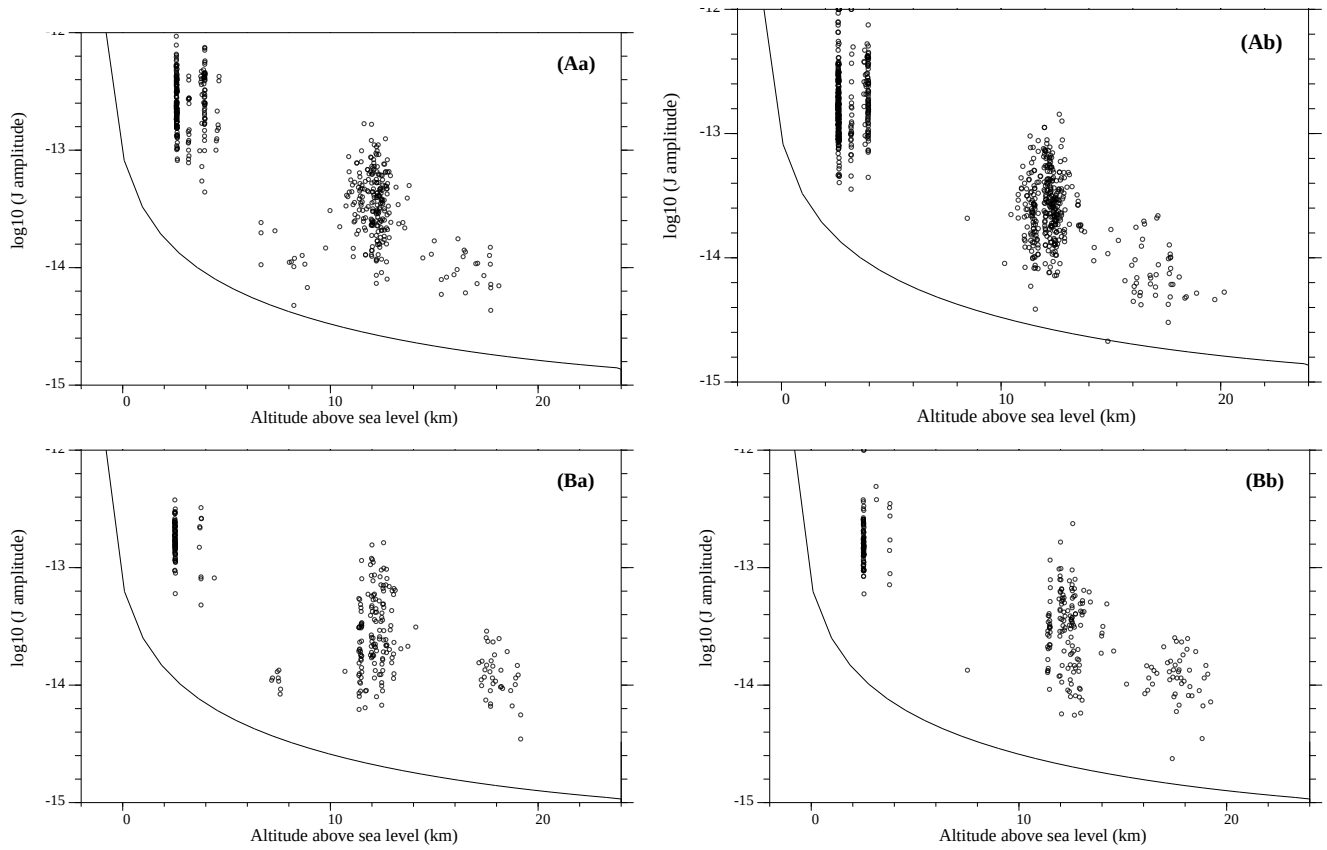


Figure II.7: Optical turbulence factors of the layers detected with automatic (a) and interactive (b) procedures for $\zeta$ Crb (A) and 95 Her (B) (open circles). The theoretical detection curve corresponding to SNR=3 is plotted as a solid line (night of 19/05/2000).

# Bibliography

*G.S.M: A Grating Scale Monitor for atmospheric turbulence measurements. II. First measurements of the wavefront outer scale at the O.C.A*
Agabi, A., Borgnino, J., Martin, F., & al., 1995, A&AS , 109, 557

*Whole atmospheric-turbulence profiling with generalized scidar*
Avila R., Vernin J., Masciadri E., 1997, Appl. Opt. 36, 7898

*Caractérisation de la turbulence atmosphérique pour la haute résolution angulaire en astronomie*
Avila R., 1998a, Ph.D. thesis, Nice University, France.

*Turbulence Profiles with Generalized SCIDAR at San Pedro Mártir Observatory and Isoplanatism Studies*
Avila R., Vernin J., Cuevas S., 1998b, PASP 110, 1106

*Atmospheric turbulence and wind profiles monitoring with generalized scidar*
Avila R., Vernin J., Sánchez L.J., 2001, A&A, 369, 364

Avila, R., et al. 2004, RevMexAA (SC), 19, 11

*Estimation of the spatial coherence outer scale relevant to long baseline interferometry and imaging in optical astronomy*
Borgnino, J. 1990, Appl. Opt., 29, 1863

*Wind and CN2 profiling by single star scintillation analysis*
Caccia J.L., Azouit M., Vernin J., 1987, Appl. Opt. 26, 1288.

Chun, M., et al. 2002, http://kolea.ifa.hawaii.edu/ mchun/mkseeing/MKSCHome.html

*Measurement of the Atmospheric Limit to Narrow Angle Interferometric Astrometry Using the Mark-Iii Stellar Interferometer*
Colavita M.M., 1994, A&A 283, 1027-1036.

*The Palomar Testbed Interferometer*
Colavita M.M., Wallace J.K., Hines B.E., et al., 1999, ApJ 501, 505.

*Wave-front temporal spectra in high-resolution imaging through turbulence*
Conan, J.-M., Rousset, G., Madec, P.-Y., 1995, JOSA, 12, 1559

Conan, R., 2000, Ph.D. thesis, Nice University, France

*Focusing on a Turbulent Layer: Principle of the "Generalized SCIDAR"*
Coulman C. E., Vernin J., Fuchs A., 1995, Appl. Opt. 34, 5461.

*Turbulence effects in narrow-angle astrometry from SCIDAR measurements at Pic du Midi*
Daigne G., Prieur J.-L., Avila R., *Astronomical site evaluation in the visible and radio range*, 13-17 November 2000, Marrakech, Morocco, Ed. J. Vernin, Z. Benkhaldoun and C. Muñoz-Tuñón, ASP Conf. Ser. 2002, Vol.266, p.142

*Forecasting and optimizing astronomic image quality using acoustic sounding*
Dubosclard G., Hecquet J., Coupinot G., Sauvageot H., 1984, A&A 140, 273-276.

*Optical resolution through a random inhomogeneous medium for very long and short exposures*
Fried D.L., 1966, JOSA, 56, 1372.

Fuchs A., Tallon M., Vernin J., 1998, PASP 110, 86.

*Comparison of optical measurements of seeing and calculations based on radiosonde data*
Hecquet J., Klauss V., 1989, A&A, 225, 585-590.

*Profiling of atmospheric turbulence strength and velocity using a generalised SCIDAR technique*
Klückers V.A., Wooder N.J., Nicholls T.W., Adcock M.J., Munro I., Dainty J.C., 1998, A&AS 130, 141-155.

*Palomar Testbed Interferometer: update*
Lane B.F., Colavita M.M., Boden A.F., Lawson P.R., 2000, SPIE 4006, 452-458.

*G.S.M.: a Grating Scale Monitor for atmospheric turbulence measurements. I. The instrument and first results of angle of arrival measurements*
Martin, F., Tokovinin, A., Agabi, A., & al. 1994, A&AS , 108, 173

*The LBT facility Scidar: Recent Results*
McKenna, D., Avila, R., Hill, J.M., Hippler, S., Salinari, P., Stanton, P., Weiss, R. 2003, in Adaptive Optics System Technologies II, P. Wizinowich and D. Bonaccini eds., Hawaii EUA, SPIE Proc. 4839, 825

*The structure of the temperature filed in a turbulent flow*
Obukhov, A.M., 1949, Izv. Akad. Nauk. SSSR, Ser. Geogr. Geofiz., 13, 58

*The PISCO speckle camera at Pic du Midi Observatory*
Prieur J.-L, Koechlin L., André C., Gallou G., Lucuix C., 1998, Experimental Astronomy, vol 8, Issue 4, p 297-315.

*SCIDAR measurements at Pic du Midi*
Prieur J.-L., Daigne G., Avila R., 2001, A&A, 371, 366–377

*Automatic determination of wind profiles with Generalized SCIDAR*
Prieur J.-L., Avila R., Daigne G., Vernin J., 2004, PASP, 116, 778–789

*Detection of atmospheric turbulent layers by spatio-temporal and spatio-angular correlation measurements of stellar-light scintillation*
Rocca A., Roddier F., Vernin J., 1974, JOSA, 64, 1000-1004.

Roddier F., 1981, *The effects of atmospheric turbulence in optical astronomy* in Progress in Optics (ed. E. Wolf), 19, 281.

*On the origin of speckle boiling and its effects i in stellar speckle interferometry*
Roddier, F., Gilli, J., & Lund, G. 1982, J. Opt. (Paris), 13, 263

*Potential of long-baseline infrared interferometry for narrow-angle astrometry*
Shao M. Colavita M.M., 1992, A&A 262, 353-358.

*Mathematical-statistical Description of the Iterative Beam Removing Technique (Method CLEAN)*
Schwarz U.J., 1978, A&A, 65, 345.

Tatarskii V.I., 1961,*Wave propagation in a Turbulent Medium*, Dover ed., New-York.

Tokovinin A.A., 1997, VLT-TRE-UNI-17416-0003, ESO, Garching.

*Measurement of seeing and the atmospheric time constant by differential scintillations*
Tokovinin A.A., 2002, Appl. Optics, 41, 957

*Comparaison Sondeur Optique/Radar VHF*
Vernin J., 1984, report, Nice University, France.

Vernin, J. 1992, in *Wave propagation in Random Media (Scintillation)*, Ed. V.I. Tatarskii, A. Ishimaru, & V.U. Zavorotny, SPIE-ISOE, Seattle, Washington, 248

*Traitement d'image adapté au speckle atmosphérique. II Analyse multidimensionnelle appliquée au diagnostic à distance de la turbulence*
Vernin J., Azouit M., 1983, J. Opt. (Paris), 14, 131.

Vernin, J., Agabi, A., Avila, R., Azouit, M., Conan, R., Martin, F., Sánchez, L., Ziad, A., 2000, *1998 Gemini Site Testing Campaign at Cerro Pachón and Cerro Tololo*, AURA Report

# Index